Approximate Models for Lateral Growth on Ice Crystal Surfaces during Vapor Depositional Growth

Jerry Y. Harrington* and Gwenore F. Pokrifka

Department of Meteorology and Atmospheric Science, The Pennsylvania State University, University Park, PA

**Corresponding author address:* Department of Meteorology and Atmospheric Science, The Pennsylvania State University, University Park, PA 16802.

E-mail: jyh10@psu.edu

ABSTRACT

Measurements show that after facets form on frozen water droplets, those facets grow laterally across the crystal surface leading to an increase in volume and surface area with only a small increase in maximum dimension. This lateral growth of the facets is distinctly different from that predicted by the capacitance model and by the theory of faceted growth. In this paper we develop two approximate theories of lateral growth, one that is empirical and one that uses explicit growth mechanisms. We show that both theories can reproduce the overall features of lateral growth on a frozen, supercooled water droplet. Both theories predict that the area-average deposition coefficient should decrease in time as the particle grows, and this result may help explain the divergence of some prior measurements of the deposition coefficient. The theories may also explain the approximately constant mass growth rates that have recently been found in some measurements. We also show that the empirical theory can reproduce the lateral growth that occurs when a previously sublimated crystal is regrown, as may happen during the recycling of crystals in cold clouds.

1. Introduction

Vapor depositional growth is largely responsible for the variety of shapes (or habits) of ice crystals found in atmospheric cold clouds. The crystal sizes, shapes, and surface properties that result from vapor growth can have strong impacts on numerical cloud model simulations of ice-containing clouds (Gierens et al. 2003; Woods et al. 2007; Avramov and Harrington 2010), on the optical properties of cloud systems (Mitchell et al. 1996; Järvinen et al. 2018; van Diedenhoven and Cairns 2020), and on the interpretation of laboratory measurements (Magee et al. 2006; Skrotzki et al. 2013; Pokrifka et al. 2020). However, quantifying the vapor growth rate of ice crystals is challenging because it is governed by two interconnected processes, namely the volume diffusion of water vapor through the background gas and the various surface processes (often called *surface kinetics*) that control the incorporation of adsorbed water molecules (ad-molecules) into the crystalline lattice. It is the combined volume diffusion and surface kinetic processes that ultimately determine the overall mass and the dimensional growth rates of crystals.

Classical growth theories treat only a single type of surface, those that are either entirely faceted or entirely rough. The classical theory of faceted growth accounts for both gas-phase diffusion and surface kinetic effects. In this theory, facets grow through the propagation of steps on their surfaces: Ad-molecules migrate across the surface as they seek suitable attachment sites such as a surface vacancy, a kink in a surface step, and so forth. Ad-molecules will incorporate into a step, and contribute to growth propagating the step forward, as long as the surface steps are sufficiently close so that a step is encountered before the ad-molecule desorbs from the surface. Classical crystal growth theory (e.g. Burton et al. 1951; Lewis 1974) employs surface models for crystals growing by steps formed through either permanent dislocations in the crystal structure or the nucleation of ”islands” on the crystal surface (step-nucleation). Most of the surface parameters required by these theories have not been measured, and so surface processes are usually treated with deposition coefficients (α) that depend strongly on ice supersaturation (hereafter supersaturation) and less-strongly on the temperature. The deposition coefficients account, in aggregate, for all of the surface processes that ultimately control the incorporation of ad-molecules into the bulk crystalline lattice. The deposition coefficients act as “growth efficiencies” taking on values between zero and unity. Though the use of deposition coefficients is relatively successful at describing the growth of faceted ice at both low and high supersaturations (Lamb and Scott 1974; Nelson and Baker 1996; Wood et al. 2001; Harrington et al. 2019), there are many processes that complicate the actual growth of crystals such as the existence of partially disordered (quasi-liquid) surface layers (Neshyba et al. 2016), the adsorption of foreign gases (Anderson et al. 1969; Knepp et al. 2009; Libbrecht and Ball 2010), phase separation that will occur upon the freezing of solution drops (Bogdan and Molina 2017), and the influence of nucleation (Pokrifka et al. 2020).

In the theory of faceted growth, the crystal dimension perpendicular to a given facet increases at a rate that depends on the vapor attachment to that facet. For instance, molecular attachment on the basal (hexagonal) face of a crystal causes the crystal dimension that is perpendicular (or normal) to that face to increase in time (see Figs. 1 and 2). We will refer to this kind of growth as *normal growth*, since molecular attachment onto the basal and prism facets causes the dimension that is perpendicular (normal) to the face to increase in time. We will also refer to the dimensions normal to the facet as the *normal dimensions* (a_n and c_n for the prism and basal facets, respectively, see Fig. 2). Most studies of crystal growth focus on normal growth, which is not surprising: Different molecular attachment rates for the basal and prism faces gives rise to the temperature variation in the primary (planar or columnar) habits of ice crystals (Lamb and Scott 1974).

Entirely rough surfaces are almost universally treated with the capacitance model, which by definition is not appropriate for faceted ice. The capacitance model explicitly assumes that the surface is a perfect sink for water vapor molecules ($\alpha = 1$), meaning that all surface processes are ignored. The vapor density is constant across the surface in the capacitance model. Consequently facets cannot remain flat (Saito 1996, pp.120-122) and the aspect ratio cannot evolve (Ham 1959).

In contrast to normal growth and rough growth, much less attention has been paid to growth that occurs laterally when facets spread across the crystal surface. This growth is distinctly different from normal growth in that the facet areas increase but often with very little increase in the normal dimensions (Fig. 1). We will refer to this kind of growth as *lateral growth*, and it can occur during ice crystal growth from the vapor (Gonda and Yamazaki 1978) and has been observed on CCl_4 crystals grown from the melt (Mayurama et al. 2000; Wettlaufer 2001). For instance, measurements show that after a supercooled droplet freezes, facets emerge on the crystal surface (see Fig. 1 of Nelson and Swanson 2019, for examples). Generally, the prism planes will appear first followed by basal planes and "rougher" conical regions in between the facets. These rougher regions develop into higher index (pyramidal) facets when the saturation state is near that of liquid, leading to a 20 faced crystal know as a "droxtal", or at lower saturation the regions may be rounded (see Gonda and Yamazaki 1978, their Fig 4.). These pyramidal regions must have high deposition coefficients ($\alpha \sim 1$) because, at higher temperatures, they grow more rapidly than the basal and prism facets (Gonda and Yamazaki 1984). Consequently, the rougher regions grow themselves out of existence leading to an increase in facet area, but with only a small increase in the normal dimensions (Gonda and Yamazaki 1984). At lower temperatures (below -25°C), the pyramidal facets may not disappear at all (Pfalzgraff et al. 2011). In fact, pyramidal facets may arise from spicules that form during droplet freezing thus producing single bullets (Magono et al. 1976). Ice crystals can, therefore, undergo growth that is influenced by two interfaces, faceted and rough, though current theories are not capable of accounting for both surface types.

Lateral growth may be important for more than the initial growth forms that develop after ice nucleation. The recent measurements of Nelson and Swanson (2019) indicate that lateral growth can lead to the production of protrusions and trapped air pockets. Their results suggest that the lateral spreading of facet protrusions is caused by adjoining surface transport, whereby molecules on the basal and prism faces migrate over facet edges and onto the protrusions. Though adjoining surface transport is theoretically unlikely (Saito 1996, pgs. 58-61), indirect evidence suggests that it occurs for thin layers (Asakawa et al. 2014). Lateral growth is also important for the growth of crystals that have previously sublimated. Sublimation causes the rounding of crystal edges leading to ellipsoidal shapes for simple planar crystals (Nelson 1998). During re-growth, facets spread across the crystal surface leading to growth rates that cannot be explained by normal growth (Nelson and Swanson 2019, their Fig. 6). Lateral growth has also been suggested as an explanation for the bending of facets that occurs during the growth of scrolls, trigonal crystals, and stacks of sheaths among other types (Nelson and Swanson 2019).

Lateral growth may also help interpret past laboratory measurements of the vapor growth of newly nucleated ice crystals. Most prior laboratory studies have used the capacitance model to interpret the measured growth rates. While the capacitance model can be made consistent with faceted growth theory (MacKenzie and Haynes 1992; Zhang and Harrington 2014), most laboratory studies include surface processes in the capacitance model with a constant deposition coefficient (e.g. Magee et al. 2006). Unfortunately, interpretations of measured growth rates using constant α lead to inconsistent results, with α values that are scattered as a function of temperature (Skrotzki et al. 2013). Pokrifka et al. (2020) suggest that these scattered results for α may be due neglected surface processes: If crystals develop facets, the deposition coefficient then depends on the supersaturation, temperature, and the crystal size. The measurements and analysis of Pokrifka et al. (2020) show that some of the scatter in the data appears to be due to variations in α predicted by the theory of faceted growth. However, Pokrifka et al. (2020) also show that a substantial number of measurements require α to decline rapidly in time, a result that cannot be explained by the theory of faceted growth. Pokrifka et al. (2020) hypothesized that the development of facets on a crystal surface could cause a rapid decline in the deposition coefficient, as rough regions are replaced by facets. Thus, a theory of lateral growth may explain laboratory growth rate measurements, and may also explain some of the scatter in prior deposition coefficient measurements.

In this paper we describe two approximate theories of lateral growth. The models treat two surface types are based on a combination of the theory of faceted growth and the theory of rough growth. We show that the models can reproduce the general features of the few available measurements on lateral spreading. We show that the time-scale for the disappearance of rough regions can be long enough to have important consequences for the interpretation of prior laboratory measurements.

2. Faceted (Normal) Growth Model

Models of faceted growth (what we call normal growth) must simultaneously account for the gas phase diffusion of water vapor and the surface kinetic processes that ultimately control the incorporation of water molecules into the crystalline lattice. Gas-phase diffusion depends on the shape of the crystal, and models of normal growth relevant for atmospheric ice assume either a cylinder (Nelson and Baker 1996) or a hexagonal prism (Wood et al. 2001) shape. These models quantify the effects of crystal shape, facet edges, and surface kinetics on the growth rate, but they require complex numerical solutions. Simplified models that account for the effects of faceted growth have also been developed using spherical (MacKenzie and Haynes 1992; Libbrecht 2003) or spheroidal (Zhang and Harrington 2014) approximations. An attractive feature of the spheroidal solution is that the theory is analytical, and the mass and dimension evolution compare well to available measurements for single crystals and to solutions from models of faceted growth (Harrington et al. 2019). It is for these reasons that we use the spheroidal model of Zhang and Harrington (2014).

In all of the models cited above, surface kinetic processes are approximated using deposition coefficients (α). Though theoretical models of α exist the parametric model of Nelson and Baker (1996) is preferable because it can, in principle, treat various surface growth modes,

$$\alpha = \alpha_s \left(\frac{s_{surf}}{s_{char}} \right)^M tanh \left(\frac{s_{char}}{s_{surf}} \right)^M . \tag{1}$$

In the above equation s_{surf} is the supersaturation immediately above the crystal surface, $s_{char}(T)$ is a temperature-dependent "characteristic" supersaturation determined from laboratory measurements (see Harrington et al. 2019), M is an empirical parameter that describes the surface growth mode, and α_s is the adsorption efficiency that is a measure of the probability that a water vapor molecule will "stick" to the surface and is assumed to be unity (Nelson 2001). In this model, α rises commensurately with s_{surf}: As the surface supersaturation increases, the density of surface steps also rises thus leading to more efficient incorporation of ad-molecules into the crystal. The increase in α with s_{surf} is controlled by both s_{char} and M (see Fig. 3). The characteristic supersaturation controls the transition from inefficient ($\alpha \sim 0$) to efficient ($\alpha \sim 1$) growth whereas the steepness of the increase in α with s_{surf} is controlled by the parameter M. A value of M = 1 in Eq. 1 is consistent with growth by permanent spiral dislocations, as originally derived by Burton et al. (1951). Though the form given above, with $M = 1$, is given by Lamb and Scott (1974). Dislocations provide a permanent source of surface steps, and produce efficient growth even at relatively low values of s_{surf}. Spiral dislocation theory presumes that the ad-molecule density on the ice surface is sparse, which is not necessarily true for atmospheric ice that may contain a very thin, partially disordered layer of surface molecules (Constantin et al. 2018). Despite this limitation, the theory appears to represent the growth of crystals by dislocations (Nelson 2005; Harrington et al. 2019). A value of $M \geq 10$ in Eq. 1 produces growth that is consistent with step nucleation (Nelson and Baker 1996). Step nucleation requires the formation of two-dimensional islands on the crystal surface and, therefore, produces a rapid onset of growth once s_{surf} is near s_{char}. These steps are generally thought to form near crystal edges where supersaturations are high and are likely responsible for the formation of very thin and symmetric crystals (Frank 1982; Wood et al. 2001).

The spheroidal solution of Zhang and Harrington (2014) assumes that the gas-phase diffusion of water vapor can be modeled with capacitance theory and that surface kinetics can be modeled with deposition coefficients, α_a and α_c, for the a and c semi-dimensions using Eq. 1. The a and c semi-dimensions are respectively referenced to half the basal facet width and half the prism height of single crystalline ice. The mass growth rate of the crystals can be computed using Eqs. 14 and 15 in Zhang and Harrington (2014), however, the Hertz-Knudsen fluxes (their Eq. 7) are more germane to the work presented here,

$$\begin{aligned} F_{as} &= \alpha_a \frac{1}{4} \overline{v}_v \left[\rho_{surf,a} - \rho_{eq}(T_i)\right] = \alpha_a \frac{1}{4} \overline{v}_v \, \rho_{eq}(T_i) \, s_{surf,a} \\ F_{cs} &= \alpha_c \frac{1}{4} \overline{v}_v \left[\rho_{surf,c} - \rho_{eq}(T_i)\right] = \alpha_c \frac{1}{4} \overline{v}_v \, \rho_{eq}(T_i) \, s_{surf,c}, \end{aligned} \tag{2}$$

where $\overline{v}_v$ is the average vapor molecule speed, $\rho_{eq}(T_i)$ is the equilibrium water vapor density at the crystal temperature, T_i, and $\rho_{surf,a}$, $\rho_{surf,c}$, $s_{surf,a}$, and $s_{surf,c}$ are the surface vapor densities and supersaturations for the subscripted axis. The vapor fluxes, F_{as} and F_{cs}, are the fluxes onto the prism and basal facets, respectively, and they are subscripted with the axis that is normal to the facet, a and c respectively. These fluxes cause the increase in the normal dimensions (a_n and c_n), and we therefore call them *normal fluxes* (Fig. 2).

The surface vapor density excess, which is the bracketed term in Eq. 2, can be written in terms of the ambient vapor density (ρ_∞) as (Eq. 9, Zhang and Harrington 2014),

$$\rho_{surf,a} - \rho_{eq}(T_i) = [\rho_\infty - \rho_{eq}(T_i)]\left(1 + \frac{\alpha_a \bar{v}_v}{4D_v}\frac{ac}{C_\Delta}\right)^{-1}$$

$$\rho_{surf,c} - \rho_{eq}(T_i) = [\rho_\infty - \rho_{eq}(T_i)]\left(1 + \frac{\alpha_c \bar{v}_v}{4D_v}\frac{a^2}{C_\Delta}\right)^{-1} \tag{3}$$

where D_v is the vapor diffusivity in air, and C_Δ is the capacitance for a spheroid of dimensions $a+\Delta$ and $c+\Delta$, and Δ is the vapor jump length at the crystal surface. The above equations for the surface vapor density and the deposition coefficients are combined with thermal diffusion and are solved iteratively (for details see Zhang and Harrington 2014) to find the fluxes F_{as} and F_{cs}.

The mass growth rate can now be found by multiplying the areas by the normal fluxes,

$$\frac{dm}{dt} = A_{bs}F_{cs} + A_{ps}F_{as} \tag{4}$$

where $A_{bs} = 4/3\pi a^2$ and $A_{ps} = 8/3\pi ac$ are the "effective" area of the spheroidal basal and prism facets, respectively (similar to Eq. 5 of Zhang and Harrington 2014). The equations for the mass growth rate and fluxes given above are for spheroidal particles, which is our proxy for faceted ice. However, the theory we develop below approximates the crystal facet areas with cylinders, and we therefore need to ensure that the growth rate computed with cylindrical areas is consistent with that of the spheroidal model. If the basal and prism cylindrical areas are denoted as $A_b = 2\pi a^2$ and $A_p = 4\pi ac$, respectively, then the above mass growth rate equation becomes,

$$\frac{dm}{dt} = A_b\left(\frac{A_{bs}}{A_b}F_{cs}\right) + A_p\left(\frac{A_{ps}}{A_p}F_{as}\right) = A_b\frac{2}{3}F_{cs} + A_p\frac{2}{3}F_{as} = A_bF_c + A_pF_a, \tag{5}$$

where F_a and F_c are the respective normal fluxes for the a and c axes: In order to be consistent with the spheroidal model, the use of cylindrical areas requires multiplication by a factor of 2/3.

3. Lateral Growth: Empirical Theory

The equations described above are valid for the normal growth of crystal faces, but they do not describe the spreading of facets shown in Fig. 1. Nelson and Swanson (2019) developed a theoretical model for lateral growth based on the migration of surface-mobile water molecules over and onto the lateral edge of the facet, thus enhancing lateral growth at the expense of normal growth. Growth measurements support this view in that the crystal normal dimensions change slowly during facet spreading (Gonda and Yamazaki 1984; Nelson and Swanson 2019). The approximate theories we develop here do not explicitly model the lateral fluxes, but use approximations that work in the correct physical manner: Lateral growth occurs at the expense of normal growth, leading to small changes in the normal dimensions.

Since no approximate theories of lateral growth exist, we begin with an idealized problem, that of an isometric crystal formed from a frozen droplet (see Fig. 2). We assume that basal and prism facets immediately begin spreading across the crystal surface, though in reality it does take time for crystal facets to emerge. This time-scale is known to depend on the supersaturation ($\sim$ 1 to 4 min. Gliki and Eliseev 1962), however, very few measurements of this time-scale exist. We therefore caution that our model will underestimate the time-scale for facet development. We assume that the facets are well approximated by circular cylinders, which simplifies the geometry considerably, and given that our theory is approximate more advanced geometry is not warranted. We assume that the pyramidal or rough regions remain as spherical sections, which is similar to observations at saturations below that of liquid (Magono et al. 1976; Gonda and Yamazaki 1978). For simplicity, we will refer to these regions as *pyramidal*.

Our development of an empirical theory for lateral growth is rooted in the measurements of Gonda and Yamazaki (1984), which are reproduced in Fig. 4. They measured the growth of basal, prism, and pyramidal facets for frozen droplets at -15°C and a supersaturation of about 1.5%. The basal and prism facet areas depend on the *lateral* a and c dimensions, defined as a_l and c_l in Fig. 2. Recall that the *overall* crystal dimensions are defined by the *normal* dimensions, a_n and c_n, which the areas and growth rates are plotted against in Fig. 4. As the figure shows, the pyramidal areas disappear as the basal and prism facet areas increase by spreading across the surface. The growth velocity of the pyramidal facets (dr/dt) increases rapidly as the area declines, however the normal growth velocities of the basal (dc_n/dt) and prism (da_n/dt) facets remain approximately constant with a slight decline as the crystal grows larger. Once the pyramidal regions are gone, a faceted hexagonal crystal remains, with the facets increasing in size by normal growth.

The growth velocities for the facet and pyramidal regions appear to be relatively independent of one another, and this suggests that an approximate theory can be constructed that treats the growth regions separately: The basal and prism faceted regions are treated with normal growth (i.e. Eq. 2), and a pyramidal region that has a rising growth velocity with declining area that suggests growth is dominated by gas-phase diffusion. In order to understand this latter point, consider a crystal that is growing by lateral growth only. In this case the normal dimensions (a_n and c_n) are constant (though the volume does increase) and so the diffusion mass flow rate to the particle will remain about the same as facets spread laterally. In order to maintain the same mass flow rate as the pyramidal area declines requires that the vapor flux to those areas (F_r) must rise, behavior that is consistent with gas-phase diffusion alone (assuming that $\alpha = 1$),

$$F_r = \frac{D_v[\rho_\infty - \rho_{surf}]}{r_r} = \frac{D_v \rho_{eq} s_i}{r_r}, \tag{6}$$

where s_i is the ambient supersaturation and r_r is an effective radial length-scale for the pyramidal area, A_r. Equation 6 is exact for a spherical particle with a radius of r_r, which suggests approximating the length scale as $r_r = [A_r/(4\pi)]^{1/2}$. This equation has the correct physical behavior in that a decline in the pyramidal area will lead to an increasing vapor flux, and therefore an increasing growth velocity since $dr/dt = F_r/\rho_i$ where ρ_i is the ice mass density. The combined mass growth rate for lateral and normal growth then becomes,

$$\frac{dm}{dt} = A_r F_r + A_b F_c + A_p F_a. \tag{7}$$

Clearly, the above equations are approximate and based on a plausible physical argument. It is worth noting that Eq. 7 may overestimate the growth rate since the flux to the pyramidal region is based on the total mass flow to the particle. This assumption is relaxed in the next section (§4).

The mass growth rate given above can now be time-stepped, however that mass must be distributed both laterally and normally. Growing the normal dimensions of the crystal is straightforward since the vapor fluxes determine the growth rates,

$$\frac{da_n}{dt} = \frac{F_a}{\rho_i}, \qquad \frac{dc_n}{dt} = \frac{F_c}{\rho_i}. \tag{8}$$

Lateral growth is treated empirically by relating changes in the total facet surface area (A_f) and pyramidal area (A_r) to changes in crystal volume: Imagine that a crystal begins growing with an initial surface area and volume of $A_\circ$ and $V_\circ$, respectively. As facets spread across the crystal, the volume and surface area will increase in time. Lateral growth will cease when the crystal volume and surface area reach that of a cylinder, or $V_{cyl} = 2\pi a_n^2 c_n$ and $A_{cyl} = 2\pi a_n^2 + 4\pi a_n c_n$. We therefore know the areas and volume of the crystal when lateral growth begins and ends, and can therefore approximate the evolution of the facet and pyramidal areas as a weighted volume fraction (w_f),

$$\begin{aligned} A_f(t) &= A_{cyl}\, w_f = A_{cyl}\left[\frac{V(t)^{2/3} - V_\circ^{2/3}}{V_{cyl}^{2/3} - V_\circ^{2/3}}\right]^n \\ A_r(t) &= A_\circ(1 - w_f), \end{aligned} \tag{9}$$

where $V(t)$ is the crystal volume at time, t. The form of w_f originates from approximating the change in surface area to volumetric changes based on a sphere, namely that $dA \propto dV^{2/3}$. We include an empirical power of n since the particle grows into a cylinder, and so we should not expect the spherical relationship to hold exactly (see below). Note that this fraction works in the correct manner in that $w_f = 0$ when the particle is entirely rough ($V(t) = V_\circ$), and $w_f = 1$ when the pyramidal regions are gone ($V(t) = V_{cyl}$).

The lateral dimensions of the crystal can now be calculated (see Fig. 2) assuming that the basal facets are tops of two circular cylinders ($A_b = 2\pi a_l^2$) and that the prism facets are given by the curved cylinder area ($A_p = 4\pi a_n c_l$),

$$A_f(t) = 2\pi a_l^2 + 4\pi a_n c_l = 2\pi a_l^2 + 4\pi a_n a_l \phi_l \tag{10}$$

where $\phi_l = c_l/a_l$ is the lateral aspect ratio which is kept constant over a time-step. The above equation is quadratic for a_l and so the solution is,

$$a_l(t) = -a_n(t)\phi_l + \frac{1}{4\pi}\sqrt{(4\pi a_n(t)\phi_l)^2 + 8\pi A_f(t)} \qquad c_l(t) = a_l(t)\phi_l. \tag{11}$$

The lateral a- and c-axis dimensions can now be determined at any time.

a. Results from Empirical Theory

The above equations were use to calculate lateral growth on a newly frozen water droplet for the data of Gonda and Yamazaki (1984) shown in Fig. 4. The equations were solved using both a small time step (Δt = 0.1 s) and using the equivalent volume sphere approach advocated by Chen (1992). In the latter approach, the growth equation is solved analytically over a time-step assuming an equivalent volume sphere of radius r_{eq}. The method is accurate, even for highly anisotropic particles, as long as the time-step is less than about 20 seconds (Harrington et al. 2013). Both methods produce indistinguishable results, and so we present the short time-step solutions. The initial diameter of the particle is taken from the data (23.8 μm), and since no information on particle aspect ratio is available we assume that c_n/a_n and c_l/a_l are both unity. The characteristic supersaturations (s_{char}) for the basal and prism facets at -15°C are taken from the fits of Harrington et al. (2019) to the measurements of Nelson and Knight (1998). Given that the growth occurred at low supersaturation (1.5%), it is reasonable to assume that dislocations were responsible ($M = 1$ in Eq. 1).

Overall, the empirical model captures the main effects of lateral and normal growth as compared to the measurements (Fig. 4). Evolution of the facet areas and the pyramidal growth velocity depend on n (Eq. 9), and though values between 2 and 3 match the data reasonably well, a value of 2.5 appears to provide the best overall match. The decline in the pyramidal area with increasing size has nearly the same functional dependence as shown by the data. Once the pyramidal area has disappeared, lateral growth ceases and the evolution of the particle is controlled by normal growth. The basal and prism areas are predicted relatively accurately during the period over which facet spreading is occurring, but both facet areas are overestimated once normal growth dominates ($2a_n > 26.5\ \mu$m). The pyramidal growth velocity increases rapidly as the diameter of the crystal rises and the pyramidal area declines, and with a similar functional dependence as expressed by the measurements. It is not surprising that the pyramidal growth velocity is most sensitive to the choice of n in Eq. 9, since the vapor flux is proportional to the inverse of the pyramidal area. The normal growth velocities of the basal and prism facets also reasonably match the measurements: The growth velocities for both facets decrease slightly as the particle diameter increases, and this is due primarily to the relatively slow decline in α of the basal and prism facets with size (Fig. 5). Since the normal growth velocities are most strongly dependent on the growth mode (M) and s_{char} through α (Eq. 1), the match of the theory with measurements provides evidence that normal growth was controlled by dislocations. This match also provides corroborating evidence for the s_{char} measured by Nelson and Knight (1998), which is important since few tests of measured s_{char} have been done at low supersaturation.

Lateral growth has a non-trivial impact on the overall mass growth rate of the crystal (Fig. 6a). The growth rate initially rises commensurately with the crystal diameter, and this is due to the increase in total surface area. However, as the pyramidal area decreases and approaches zero (near $2a_n \sim 26.5\ \mu$m), the mass growth rate begins to flatten. This result is due to the declining mass uptake of the pyramidal regions as their area shrinks to zero. The disappearance of the pyramidal regions takes about 3 minutes (Fig. 6b), which occurs when the lateral facet a-axis dimension (a_l) approaches the normal a-axis dimension (a_n). This time-scale is similar to the measured range of 2 to 4 minutes (Gonda and Yamazaki 1984). The loss of the pyramidal regions causes the total mass growth rate to asymptotically approach the normal growth rate, as expected.

In order to provide context for the total mass growth rate, calculations using rough growth and using the spherical capacitance model are also shown. Rough growth provides the maximum rate and it was computed diagnostically: As the crystal evolved, the rough growth rate was calculated assuming that $\alpha = 1$ for the entire crystal, but this growth rate did not influence the particle evolution. The rough growth rate initially follows, but then climbs away from, the total growth rate. This difference with the total growth rate occurs because the average α declines as the particle becomes faceted (Fig. 5), causing the total mass growth rate to fall.

The capacitance model calculations followed the standard approach of treating the crystal as a sphere with $\alpha = 1$. Treating the crystal in this manner leads to mass growth rates that are initially lower than the total growth rate (Fig. 6), a result that is due to spherical particles having too small of a surface area for a given volume. The measured crystals grow by filling out volume and increasing area while the normal dimension changes slowly. Once lateral growth ceases, a fully faceted crystal remains with an area-average α value below unity (Fig. 5). In contrast, the larger capacitance growth rate causes the size to increase more rapidly than that of the faceted crystal (Fig. 6b), and this in turn increases the growth rate. As discussed in the introduction, it is common practice to adjust the capacitance model using a constant α in order to match the mass growth measured in laboratory experiments. If that approach were applied to a crystal undergoing lateral growth, such as the case considered above, an α of approximately 0.05 (Fig. 6a) would be needed to match the mass growth. This value is too low in comparison to the time-series of α, which is generally above 0.1, and mis-represents the actual growth process.

4. Lateral Growth: Mechanistic Theory

The empirical theory above is relatively successful at reproducing the measured growth rates of a combination of basal and prism facets and pyramidal regions. However, the theory is based on the assumption that the vapor flux to the pyramidal regions can be treated classically, and that the facet areas increase commensurately with the volume. In this section we develop a mechanistic model that links these two assumptions to surface kinetic effects. Doing so entails some key assumptions, though the results are not overly sensitive to those assumptions.

a. Attachment kinetics with basal, prism, and pyramidal regions

As discussed in the introduction, we use deposition coefficients to model all surface kinetic processes. Given the generally larger growth velocity of the pyramidal regions due to lateral growth, we represent this growth with a higher deposition coefficient (α_r) than the basal (α_c) and prism (α_a) facets. This representation of α_r is supported by molecular dynamics simulations (Pfalzgraff et al. 2011) that show higher α for the pyramidal facets. Calculating α_r using Eq. 1 requires an s_{char} for the pyramidal region; since the growth of this region is highly efficient we represent it with an $s_{char,r}$ that is a factor f_{char} lower than the smallest value among the basal and prism facets,

$$s_{char,r} = f_{char} \cdot min(s_{char,a}, s_{char,c}) \quad \text{where} \quad f_{char} < 1 \tag{12}$$

The adjustable parameter f_{char} is used to mimic the combine effects of direct and adjoining surface fluxes on lateral growth (Fig. 2).

The mass growth equation (Eq. 7) remains the same, except that the vapor flux to the pyramidal region is now treated similarly to the vapor flux to the basal and prism faces of the crystal (Eq. 2), however with an important modification. Instead of treating the surface vapor density with distinct values for each facet, we assume that growth is driven by a single value of ρ_{surf}. This is an oversimplification, but as a first approximation it may be justified: If lateral growth dominates the vapor uptake, then the pyramidal regions will reduce s_{surf} keeping its value low and nearly the same at the edge of both the basal and prism facets (as indicated in Fig. 2). Consequently, the basal and prism normal growth rates will be reduced with the result that mass will be preferentially deposited in the pyramidal regions, thus causing facet spreading. Using the assumption that ρ_{surf} is the same for each crystal facet in Eq. 2, the mass growth rate (Eq. 7) can be written as,

$$\frac{dm}{dt} = A_r F_r + A_b F_c + A_p F_a = A_t \, \overline{\alpha} \, \frac{1}{4} \, \overline{v}_v \, [\rho_{surf} - \rho_{eq}(T_i)] \tag{13}$$

where $A_t = A_r + A_b + A_p$ is the total surface area, and $\overline{\alpha} = \frac{A_p}{A_t}\alpha_a + \frac{A_b}{A_t}\alpha_c + \frac{A_r}{A_t}\alpha_r$ is the area averaged deposition coefficient.

The above surface kinetic equation must now be coupled with the ambient gas-phase diffusion of water vapor to the crystal, and we use capacitance theory following Zhang and Harrington (2014),

$$\frac{dm}{dt} = 4\pi C_\Delta D_v [\rho_\infty - \rho_{surf}], \tag{14}$$

where the above symbols were previously defined. The vapor transport rate from the far field (Eq. 14) must match the transport at the surface (Eq. 13), allowing us to solve for $\rho_{surf} - \rho_{eq}$,

$$\rho_{surf} - \rho_{eq}(T_i) = [\rho_\infty - \rho_{eq}(T_i)] \left(1 + \frac{\overline{\alpha}\,\overline{v}_v}{4D_v} \, \frac{A_t}{4\pi C_\Delta}\right)^{-1} = \frac{[\rho_\infty - \rho_{eq}(T_i)]}{1 + R_k}. \tag{15}$$

This equation has the same form as that for normal growth (Eq. 3), except that the axis-dependent α are replaced with the area-average. The denominator of the right-hand-side of the equation can be interpreted as a “surface resistance”, R_k: As the $\overline{\alpha}$ declines, the surface resistance to growth increases causing a rise in the surface vapor density and supersaturation. We expect this physical behavior to occur during lateral growth, when the more efficiently growing pyramidal regions are replaced with slower growing facets. Combining Eqs. 14 and 15 gives the equation for mass growth in terms of the ambient and equilibrium vapor densities,

$$\frac{dm}{dt} = 4\pi C D_v^*[\rho_\infty - \rho_{eq}(T_i)] \qquad \text{where} \qquad D_v^* = \frac{D_v}{\frac{C}{C_\Delta} + R_k}. \tag{16}$$

Mass growth including surface kinetics are often cast in a similar form (see Lamb and Verlinde 2011, pg. 337). Thermal diffusion is treated following Zhang and Harrington (2014) and, for brevity, will not be repeated here.

b. Mass and axis length prediction

Using the mass growth rate above requires specific geometrical details. For instance, Fig. 2 shows that the normal fluxes to the basal and prism facets cause the outward growth of the normal dimensions (a_n and c_n), as shown by the blue rectangles in Fig. 7. The combination of direct fluxes and adjoining surface fluxes to the pyramidal regions will cause the pyramidal axis (p_n) and the lateral facet axes (a_l and c_l) to increase in time. It is possible to attack this problem by calculating the height of the facets above the pyramidal regions and then growing the facets laterally using explicit fluxes (the approach of Nelson and Swanson 2019). We have developed a model of this growth, however it is complex and requires a number of additional assumptions. A more rudimentary approach is taken here that produces qualitatively similar results. If we assume that there is no height to the basal and prism facets, then the round regions directly intersect the facets (Fig. 7). Since α of the pyramidal regions is always greater than that of the basal and prism facets, the outward growth of the pyramidal region is always sufficient for the edges to intersect.

However, requiring the intersection of the round and facet regions means that the pyramidal region grows at a faster rate than is measured (see below).

Requiring the intersection of the facets and the round regions makes it possible to analytically calculate the changes in the normal axis lengths (a_n, c_n, and p_n) and the lateral facet dimensions (a_l and c_l) if we know the area and volume. The total surface area of the basal, prism, and pyramidal regions can be computed directly from the lateral and normal dimensions using the geometry in Fig. 7,

$$\begin{aligned} A_b &= 2\pi a_l^2, \\ A_p &= 4\pi a_n c_l, \\ A_r &= 2\int_0^{2\pi}\int_{\phi_a}^{\phi_c} p_n^2\, sin\phi\; d\phi\; d\theta = 4\pi p_n^2\,[cos\phi_a - cos\phi_c] = 4\pi p_n\,[c_n - a_l], \end{aligned} \tag{17}$$

where the last equation uses $cos(\phi_a) = c_n/p_n$ and $cos(\phi_c) = a_l/p_n$, and it assumes spherical sections that therefore restricts this model to isometric crystals ($a_n = c_n$ and $a_l = c_l$).

The total volume can also be calculated analytically based on the geometry of Fig. 7. One can integrate from $\phi = 0$ to $\phi = \phi_a$ over the flat basal region which gives the volume of a cone (V_b), then over the circular region from $\phi = \phi_a$ to $\phi = \phi_c$ which gives the volume of a spherical section (V_r), and finally from $\phi = \phi_c$ to $\phi = \pi/2$ over the flat prism region (V_p) resulting in,

$$\begin{aligned} V_b &= \frac{2}{3}\pi a_l^2 c_n, \\ V_r &= \frac{4}{3}\pi p_n^3\,[cos\phi_a - cos\phi_c] = \frac{4}{3}\pi(c_n^2 + a_l^2)\,[c_n - a_l], \\ V_p &= \frac{4}{3}\pi a_n^2 c_l, \\ V_t &= V_r + V_b + V_p = \frac{4}{3}\pi\,\left[(c_n^2 + a_l^2)(c_n - a_l) + \frac{1}{2}a_l^2 c_n + a_n^2 c_l\right], \end{aligned} \tag{18}$$

where the last equation is the total volume of the crystal and $p_n^2 = c_n^2 + a_l^2$ has been used. Note that V_t has the correct limiting behavior for an isometric crystal ($a_n = c_n$). Initially the crystal is spherical without any facets, and so $a_l = c_l = 0$, and the total volume reduces to that of a sphere.

If the crystal remains isometric and the pyramidal regions grow themselves out of existence, then $a_n = c_n = a_l = c_l$ and the volume becomes that of a cylinder ($2\pi a_n^2 c_n$).

It is now possible to calculate the change in the mass and volume of the crystal, and hence the normal and lateral dimensions. As in §3 the total mass, $m(t+\Delta t)$, and total volume, $V_t(t+\Delta t) = m(t+\Delta t)/\rho_i$, at the end of a short time-step ($\Delta t = 0.1s$) can be computed directly from the mass growth equation (Eq. 16) with thermal diffusion included. Similarly, the normal dimensons at the end of a time-step, $a_n(t+\Delta t)$ and $c_n(t+\Delta t)$, can be computed directly from Eq. 8. To keep the particle isometric we use the average of the a_n and c_n growth velocities during lateral growth only. The lateral dimensions cannot be determined in a similar fashion. However, since the total volume and the normal dimensions are known at the end of the time-step, the new lateral dimensions can be found diagnostically. Equation 18 can be rearranged as,

$$V_t(t+\Delta t) = \frac{4}{3}\pi \left[-a_l^3 + \frac{3}{2} c_n a_l^2 + (a_n^2 \phi_l - c_n^2) a_l - c_n^3 \right]_{t+\Delta t}, \tag{19}$$

where every term on the right-hand-side is at the end of the time-step ($t+\Delta t$). This is a cubic equation for the lateral dimension, a_l, which is the only unknown. Standard cubic solutions can be used to find a_l and this closes the equation set.

c. Results from Mechanistic Theory

The mechanistic theory was used evolve the frozen droplet described §3, however the deposition coefficient (α_r) for the pyramidal region is needed and this requires specifying f_{char} (Eq. 12). We used a wide range of f_{char} in our simulations, from 1/3 to 1/10, but found that the main features of lateral growth remained the same, and that a value of f_{char} = 1/5 produces the best match to the data. The evolution of the areas and growth velocities (Fig. 8) is similar to that produced by the empirical model, in that a rapid increase in the basal and prism areas occurs, along with a commensurate decline in the pyramidal area. Once lateral growth ceases, and the pyramidal area is gone (near $2\,a_n$ = 26 μm), the basal and prism facets grow more slowly at their normal growth rates. The pyramidal area disappears faster in the mechanistic theory, a result that is likely due to the requirement that the round and facet regions intersect. Unlike the empirical model, the mechanistic model more accurately captures the evolution of the facet areas. What is most remarkable about the mechanistic theory calculations is that the prism area matches the data with high precision even during the period of lateral growth. Both basal and prism facet areas are exceedingly well predicted after lateral growth ceases, a result that strongly suggests the facets grew with dislocations at the measured s_{char} of Nelson and Knight (1998).

The growth velocities of the pyramidal region and a-axis match the measurements, though the c-axis growth rate is under-predicted. Note that all of the growth velocities increase during facet spreading, which qualitatively agrees with the measurements. The physical cause of this increase is the competition for vapor among the surface regions. When the basal and prism facets are small, the pyramidal region keeps the surface supersaturation low (Fig. 9) due to that region's higher α_r thus starving the facets of vapor. This result is expected based on the work of Nelson and Swanson (2019), though in their theory explicit adjoining surface fluxes rob the facets of vapor at the expense of lateral growth. No surface process is explicitly modeled in the theory presented here, and instead α_r for the pyramidal region acts in an aggregate fashion to mimic the reduction of the basal and prism facets normal growth. As the basal and prism facets spread laterally, and the pyramidal area declines, the surface supersaturation rises causing an increase in α_a, α_c, and α_r (Fig. 9). Even though the individual α increases, the area-averaged value ($\overline{\alpha}$) decreases due to the declining pyramidal area: The pyramidal region is being replaced by slower-growing basal and prism facets with lower α. Once the pyramidal region is gone, s_{surf} declines as the particle increases more rapidly in size and grows by normal growth alone. The link between s_{surf} and α_r is the primary reason for the sensitivity of the areas and growth velocities to our choice of

f_{char} (shown as the shaded regions on the figures). Nevertheless, the qualitative features of lateral growth are not strongly dependent on the choice of f_{char}. Indeed, the cessation of facet spreading, which occurs when a_l equals the normal axis length a_n, occurs after 2 minutes with a spread of 30 seconds due to our selected range of f_{char} (Fig. 10b).

The evolution of the growth velocities is reflected in the total mass growth rate of the crystal (Fig. 10a). Mass growth is initially dominated by lateral growth, which declines rapidly with crystal diameter. As the basal and prism facet areas increase, thus replacing the pyramidal regions, the normal growth rate rises until it dominates the total growth rate. Unlike the empirical model, the mechanistic theory does not produce a maximum in the total growth rate during facet spreading (Fig. 10) because s_{surf} rises smoothly in time. Furthermore, the evolution of s_{surf} is responsible for the greater growth rate produced by the mechanistic model once lateral growth ceases. The use of a single s_{surf} leads to a larger α_a and a smaller α_c (Figs. 5 and 9), more rapid a-axis growth and, in turn, a higher mass growth rate than the empirical model. If we followed the common procedure of adjusting the capacitance model with a constant α in order to match the actual growth rate, a value of 0.075 would be needed. Again, this procedure is often used to interpret laboratory measurements of mass growth. If lateral growth is occurring on the measured crystals the value of α determined from the measurements could be too low and it would mis-represent the actual growth process.

5. Implications of Lateral Growth

The results from sections 3 and 4 indicate that lateral growth may depend on initial size. Facets must spread laterally over a greater area on a crystal that has a larger initial size. Consequently, the time-scale over which lateral growth occurs (τ_l), and over which the normal dimension is approximately constant, should increase with the initial size of the crystal. Figure 11 shows that this is indeed the case for two crystals grown at a supersaturation of 10%, a temperature of -40°C, and a pressure of 1000 hPa. Smaller crystals with diameters typical of most cloud droplets (20 μm) have lateral growth time-scales on the order of a few minutes, whereas for larger crystals (diameter 40 μm) the time-scale can be 10s of minutes. Simulations conducted over a range of supersaturations and initial particle sizes indicate that τ_l is generally on the order of 1 to 10 minutes for most crystals with initial diameters in the range of 20 to 60 μm. These time-scales are long enough that ice-containing clouds could be impacted by lateral growth, and these results may bear on prior laboratory studies of crystal growth, which we turn to next.

The experiments of Pokrifka et al. (2020) showed that a number of the small (radius $\sim$ 10 μm), homogeneously-frozen crystals grown in their electrodynamic diffusion chamber could not be modeled with constant α or with normal growth. Those growth data could only be explained if α decreased in time, which is similar to the behavior predicted by lateral growth (Figs. 5 and 9). Pokrifka et al. (2020) suggested facet spreading as one possible way to explain the data, and they provided an *ad hoc* method to model the measurements. Detailed fits to their data are beyond the scope of this work, though it is worthwhile to ask whether the theory developed here produces results that are comparable to those measurements. A useful measure of the overall mass growth invoked by Pokrifka et al. (2020), and used in other studies (Swanson et al. 1999; Harrison et al. 2016), is that of a power-law,

$$\frac{dm}{dt} = A_t F_{vapor} \propto r^p, \tag{20}$$

where A_t is the total particle area, F_{vapor} is the vapor flux to the crystal, and r is the radius assuming the crystal is isometric. That the growth rate is proportional to r^p can be seen if two limits are considered. Under diffusion-limited growth (capacitance model) $p = 1$ because the surface provides no resistance to growth ($\alpha = 1$), and the vapor flux is proportional to the inverse of the radius (Eq. 6). Under kinetics-limited growth the surface resistance is large causing the gas-phase vapor gradient and the size-dependence of the vapor flux to disappear (as in Eq. 2) leading to $p = 2$. Normal growth has power law exponents that range between 1 and 2, and some of the data of Pokrifka et al. (2020) follow this growth (their Fig. 12 and our Fig. 12). However, approximately half of the measured crystals grew slowly, produced $p < 1$, and required α that decline in time in order to fit the data. We did representative calculations using lateral growth theory with typical frozen droplet radii (10 and 20 μm), temperature (-40°C), pressure (970 hPa), and supersaturation (10%) of the experiments. The value of p was calculated from the slope of the mass derivative and the mass in log-log space, following Pokrifka et al. (2020), their Eq. 14. Note that both the empirical and mechanistic models produce $p < 1$ along with curve shapes that resemble those derived from the data (Fig. 12). The empirical model produces a lower value of p, and this is due to the longer period of time over which the growth rate remains relatively constant. The initial size also produces a lower value of p (shaded range in Fig. 12) since larger particles have longer periods of lateral growth (Fig. 11). These results provide some additional evidence that lateral growth may have been captured in the experiments of Pokrifka et al. (2020), though their mechanism assumed a transition to step nucleation growth whereas the model developed here suggests dislocations can also explain the data.

These experiments also provide some tantalizing evidence for an initial size dependence to growth. If the average values of p from the experiments (Fig. 13 of Pokrifka et al. 2020) are plotted against the initial particle size, a slight size dependence emerges (Fig. 13). While there is not enough data to draw definitive conclusions, the data suggest that p may be lower for crystals formed from initially larger frozen droplets. The average p-values derived from the empirical model produces curves with a roughly similar initial size dependence to the data, using a similar temperature and pressure from of those experiments (-40°C and 970 hPa, respectively). The maximum and minimum range of p determined from the simulations (grey shade) are also on the order of those derived from the measurements (error bars), and supersaturation plays only a modest role in determining the curve shape. While the empirical model indicates an intriguing initial size dependence to p, such a dependence does not appear in the mechanistic model. The reason for this difference is due to the manner in which the mass growth rate evolves during facet spreading. The empirical model produces a small maximum with a constant rate thereafter until lateral growth ceases, whereas the mechanistic model produces a rise in the growth rate throughout the period of lateral growth (Fig. 10). With so little data it is not possible to draw specific conclusions and more measurements of lateral growth are needed.

Lateral growth is also known to occur on previously sublimated crystals, and this growth may be important for crystals cycled in cold clouds. Nelson and Swanson (2019) measured the lateral growth of the basal facet on a previously sublimated crystal at T = -30°C, a supersaturation of about 1%, and at atmospheric pressure (Fig. 14). Their results showed that the ratio of the lateral to the normal basal radius ($\phi_a = a_l/a_n$) increased rapidly initially, but slowed down as the facet spread across the surface. Normal growth cannot explain the data and a lateral growth model is required (Nelson and Swanson 2019, their Fig. 6). While the mechanistic model developed here is only valid for isometric crystals, the empirical model is capable of modeling non-isometric growth since it was developed based on the spheroidal model of Zhang and Harrington (2014). The measured crystal had a basal axis radius of about a_n = 186 μm, and we assumed an initial crystal thickness of 60 μm which is similar to the measured crystals. The s_{char} for normal growth were taken from the data set of Harrington et al. (2019), and the empirical model results are shown in Fig. 14 for three different supersaturations (1, 2 and 3%). Clearly, the empirical model captures the increase in the axis length ratio in time, including the more rapid initial spreading of the facets and the later slow-down in the growth. While the measured supersaturation was 1%, our model requires higher values of 2 to 3% for a better match with the data. In addition, the data indicate that the normal a-dimension (a_n) increased by 1 μm, whereas the empirical model produces a nearly 6 μm increase in a_n. Never-the-less, the qualitative match with the data is encouraging especially if one bears in mind the simplistic nature of the empirical theory. The slow-down in growth is also reflected in the mass growth rate (Fig. 14b), which shows an initial rise followed by a plateau and a minor decrease towards the end of the simulation. It is worth noting that mass derivatives with this shape have been measured (Pokrifka et al. 2020, their Fig. 11b). If we treated the crystal with normal growth only, the growth rate would be too low by about 30% (Fig. 14b). On the other hand, treating the crystal as if it were entirely rough ($\alpha = 1$, capacitance model) would produce mass growth that rapidly diverges from the actual growth rate and becomes too large.

6. Concluding Remarks

Growth that spreads laterally across crystal surfaces has not often been measured, but it may have important consequences for ice-containing clouds and laboratory measurements of ice crystal growth. If our simple theory is approximately correct, then lateral growth produces rates that are initially higher, but then become generally lower than that predicted by capacitance theory and this is due to two factors: Efficiently growing regions are replaced by facets that grow with lower efficiency, leading to a declining area-averaged deposition coefficient ($\overline{\alpha}$) in time and a lower growth rate. But this decrease in $\overline{\alpha}$ is also conflated with the changing particle geometry. The particle is growing, essentially, by filling out volume and increasing surface area while the particle normal dimension increases slowly in time until lateral growth ceases. These process will also be modulated by the time-scale for initial facet formation, for which few studies exist. Lateral growth may therefore complicate interpretations of laboratory-grown ice crystals, especially those that include nucleation. For instance, many studies of surface kinetics at low temperatures (below -30°C) have used small ice crystals and the spherical capacitance model with a constant $\overline{\alpha}$ (Magee et al. 2006; Skrotzki et al. 2013; Harrison et al. 2016). However, the assumption of a constant α for ice is only approximately true if the surface structure is static in time, which is not the case for actively growing ice (Nelson 2005). If both lateral and normal growth are occurring on the growing crystals the estimated $\overline{\alpha}$ could then be either too low or too high depending upon the initial size of the crystal, the length of the measurement, and the supersaturation. Longer growth experiments at low to moderate supersaturations on cloud-droplet sized crystals could lead to anomalously low estimates of $\overline{\alpha}$ (as indicated in Figs. 6 and 10). On the other hand, short-duration experiments could lead to anomalously high values of $\overline{\alpha}$ if an active period of lateral and normal growth is sampled since the growing crystals are not changing much in size, but instead are growing by filling out surface area and volume.

Crystals that are cycled through periods of growth and sublimation may also be influenced by lateral growth, and this could help explain some perplexing results from laboratory studies. The levitation cloud chamber studies of Magee et al. (2006) required low α to explain their results. Their crystals were cycled between growth and sublimation, so it could be that lateral growth occurred frequently in their studies, which would then affect the deposition coefficients determined by those studies. A recent study by Voigtländer et al. (2018) showed increasing optical complexity likely associated with mesoscopic and other larger surface features as crystals were cycled through growth and sublimation regimes. The growth of the crystals seemed to become suppressed by such cycling, and this could be an indication of contributions from lateral growth.

Lateral growth may also have consequences for the microphysics of cold clouds. If facet spreading dominates the early growth of crystals it could influence the nucleation of ice in some types of cirrus clouds. The concentration of crystals in cirrus depend on the manner in which ice is nucleated, and the homogeneous freezing of solution droplets can produce high concentrations of ice crystals. However, homogeneous freezing is sensitive to the ambient supersaturation; the growth of pre-existing crystals and newly frozen solution droplets are a sink of water vapor, which can cause a reduction in the rate of homogeneous freezing (e.g. DeMott et al. 1997). Active lateral growth on newly frozen solution droplets could initially enhance vapor growth (through increased surface area), leading to further suppression of homogeneous freezing. The dynamic recycling of crystals through clouds could also be influenced by lateral growth. Larger crystals that sublimate below cloud base and are recycled by stronger updrafts could see relatively long periods of lateral growth. Such periods of lateral growth may produce relatively constant growth rates, along with maximum dimensions that change slowly in time thus affecting crystal fall speeds. Finally, Nelson and Swanson (2019) suggest that many of the complex ice features at low temperature (below -30°C) are influenced by lateral growth, and this may indicate that theories of ice vapor growth for very cold clouds need to be revised.

Acknowledgments. The authors are grateful for support from the National Science Foundation under Grant #AGS-1824243. The authors benefited from conversations with Drs. Alexei Korolev, Alfred Moyle, and Jon Nelson. Three anonomous reviewers are thanked for comments that improved this article.

Data Statement: Raw growth data used to produce the Figs. 12 and 13 are available from Data Commons, The Pennsylvania State University (Pokrifka et al. 2018). The crystal growth data used in Fig. 13 were kindly provided by Dr. Jon Nelson. The data from Gonda and Yamazaki (1984) were extracted from their figures using the software, Engauge Digitizer. Simulation output and data used to produce the figures are available from Data Commons at https://doi.org/10.26208/4a9x-p796

References

Anderson, B., J. Sutkoff, and J. Hallett, 1969: Influence of methyl 2-cyanoacrylate monomer on the habit of ice crystals grown from the vapor. *J. Atmos. Sci.*, **26**, 673–674.

Asakawa, H., G. Sazaki, E. Yokoyama, K. Ngashima, and S. Nakatsubo, 2014: Roles of surface/volume diffusion in the growth kinetics of elementary spiral steps on ice basal faces grown from water vapor. *Cryst. Growth Des.*, **14**, 3210–3220.

Avramov, A., and J. Harrington, 2010: The influence of parameterized ice habit on simulated mixed-phase arctic clouds. *J. Geophys. Res.*, **115**, D03 205.

Bogdan, A., and M. Molina, 2017: Physical chemistry of the freezing process of atmospheric aqueous drops. *J. Phys. Chem.*, **121**, 3109 – 3116.

Burton, W. K., N. Cabrera, and F. C. Frank, 1951: The growth of crystals and the equilibrium structure of their surfaces. *Philosophical Transactions of the Royal Society of London. Series A, Mathematical and Physical Sciences*, **243 (866)**, 299–358.

Chen, J.-P., 1992: Numerical Simulation of the Redistribution of Atmospheric Trace Chemicals Through Cloud Processes. Ph.D. thesis, The Pennsylvania State University, University Park, PA, 16802, 342pp.

Constantin, J., M. Gianetti, M. Longinotti, and H. Corti, 2018: The quasi-liquid layer of ice revisited: The role of temperature gradients and tip chemistry in AFM studies. *Atmos. Chem. Phys.*, **18**, 14 965–14 978.

DeMott, P., D. Rogers, and S. Kreidenweis, 1997: The suceptibility of ice formation in upper tropospheric clouds to insoluble aerosol components. *J. Geophys. Res*, **102**, 19 575–19 584.

Frank, F. C., 1982: Snow crystals. *Contemporary Physics*, **23 (1)**, 3–22, doi:10.1080/00107518208231565.

Gierens, K., M. Monier, and J.-F. Gayet, 2003: The deposition coefficient and its role for cirrus. *J. Geophys. Res.*, **108(D2)**, 4069.

Gliki, N., and A. Eliseev, 1962: Effects of supersaturation and temperature on the development kinetics of the initial growth forms on a sphere of ice. *Kristallografiya*, **7**, 802–804.

Gonda, T., and T. Yamazaki, 1978: Morphology of ice droxtals grown from supercooled water droplets. *J. Cryst. Growth*, **45**, 66–69.

Gonda, T., and T. Yamazaki, 1984: Initial growth forms of snow crystals growing from frozen cloud droplets. *J. Meteorol. Soc. Japan*, **62**, 190–192.

Ham, F., 1959: Shape-preserving solutions of the time-dependent diffusion equation. *Quarterly of Applied Mathematics*, **17 (137-145)**.

Harrington, J., K. Sulia, and H. Morrison, 2013: A method for adaptive habit prediction in bulk microphysical models. Part I: Theoretical development. *J. Atmos. Sci.*, **70**, 349–364, doi:10.1175/JAS-D-12-040.1.

Harrington, J. Y., A. Moyle, L. E. Hanson, and H. Morrison, 2019: On calculating deposition coefficients and aspect-ratio evolution in approximate models of ice crystal vapor growth. *Journal of the Atmospheric Sciences*, **76 (6)**, 1609–1625, doi:10.1175/JAS-D-18-0319.1.

Harrison, A., A. Moyle, M. Hanson, and J. Harrington, 2016: Levitation diffusion chamber measurements of the mass growth of small ice crystals from vapor. *J. Atmos. Sci.*, **73**, 2743–2758.

Järvinen, E., and Coauthors, 2018: Additional gobal climate cooling by clouds due to ice crystal complexity. *Atmos. Chem. Phys.*, **18**, 15 767–15 781.

Knepp, T., T. Renkens, and P. Shepson, 2009: Gas phase acetic acid and its qualitative effects on snow crystal morphology and the quasi-liquid layer. *Atmos. Chem. Phys.*, **9**, 7679–7690.

Lamb, D., and W. Scott, 1974: The mechanism of ice crystal growth and habit formation. *J. Atmos. Sci.*, **31**, 570–580.

Lamb, D., and J. Verlinde, 2011: *Physics and Chemistry of Clouds*. Cambridge University Press, New York, 584 pp.

Lewis, B., 1974: The growth of crystals of low supersaturation. I. Theory. *J. Cryst. Growth*, **21**, 29–39.

Libbrecht, K., 2003: Growth rates of the principal facets of ice between -10°C and -40°C. *J. Crystal Growth*, **247**, 530–540.

Libbrecht, K., and R. Ball, 2010: Chemical influences on ice crystal growth from vapor. *arXiv Materials Science*, arXiv:1101.0127.

MacKenzie, A., and P. Haynes, 1992: The influence of surface kinetics on the growth of stratospheric ice crystals. *J. Geophys. Res.*, **97**, 8057–8064.

Magee, N., A. Moyle, and D. Lamb, 2006: Experimental determination of the deposition coefficient of small cirrus-like crystals near -50 °C. *Geophys. Res. Let.*, L17813.

Magono, C., S.-I. Fujita, and T. Taniguchi, 1976: Shapes of single crystals originated from frozen cloud droplets. *International Conference on Cloud Physics*, 26 - 30 July, Boulder Colorado, 103-106.

Mayurama, M., N. Kuribayashi, K. Kawabata, and J. Wettlaufer, 2000: Shocks and curvature dynamics: A test of global kinetic faceting in crystals. *Phys. Rev. Lett.*, **85**, 2545–2548.

Mitchell, D. L., A. Macke, and Y. Liu, 1996: Modeling cirrus clouds. Part II: Treatment of radiative properties. *J. Atmos. Sci.*, **53**, 2967–2988.

Nelson, J., 1998: Sublimation of ice crystals. *J. Atmos. Sci.*, **55**, 910–919.

Nelson, J., 2001: Growth mechanisms to explain the primary and secondary habits of snow crystals. *Philos. Mag. A.*, **81**, 2337–2373.

Nelson, J., 2005: Interactive comment on "supersaturation dehydration, and dentrification in arctic cirrus". *Atmos. Chem. Phys. Discuss.*, **5**, S257–S260.

Nelson, J., and M. Baker, 1996: New theoretical framework for studies of vapor growth and sublimation of small ice crystals in the atmosphere. *J. Geophys. Res.*, **101**, 7033–7047.

Nelson, J., and C. Knight, 1998: Snow crystal habit changes explained by layer nucleation. *J. Atmos. Sci.*, **55**, 1452–1465.

Nelson, J., and B. Swanson, 2019: Lateral facet growth of ice and snow – Part 1: Observations and applications to secondary habits. *Atmospheric Chemistry and Physics*, **19**, 15 285–15 320.

Neshyba, S., J. Adams, K. Reed, P. M. Rowe, and I. Gladich, 2016: A quasi-liquid mediated continuum model of faceted ice dynamics. *Journal of Geophysical Research: Atmospheres*, **121 (23)**, 14,035–14,055, doi:10.1002/2016JD025458.

Pfalzgraff, W., S. Neshyba, and M. Reselova, 2011: Comparative molecular dynamics study of vapor-exposed basal, prismatic, and pyramidal surfaces of ice. *J. Phys. Chem.*, **115**, 6184–6193.

Pokrifka, G., A. Moyle, L. Hanson, and J. Harrington, 2020: Estimating surface attachment kinetic and growth transition influences on vapor-grown ice crystals. *J. Atmos. Sci.*, **77**, 2393–2410.

Pokrifka, G., A. Moyle, and J. Y. Harrington, 2018: Electrodynamic levitation diffusion chamber measurements of the mass growth of homogeneously-nucleated ice crystals grown from the vapor. Penn State Data Commons https://doi.org/10.26208/z7bf-nq20.

Saito, Y., 1996: *Statistics Physics of Crystal Growth*. World Scientific, 179pp.

Skrotzki, J., and Coauthors, 2013: The accommodation coefficient of water molecules on ice - cirrus cloud studies at the AIDA simulation chamber. *Atmos. Chem. Phys.*, **13**, 4451–4466.

Swanson, B. D., N. Bacon, E. J. Davis, and M. B. Baker, 1999: Electrodynamic trapping and manipulation of ice crystals. *Quart. J. Roy. Meteor. Soc.*, **125**, 1039–1058.

van Diedenhoven, B., and B. Cairns, 2020: A flexible parameterization for shortwave and long-wave optical properties of ice crystals and derived bulk optical properties for climate models. *J. Atmos. Sci.*, **77**, 1245–1260.

Voigtländer, J., and Coauthors, 2018: Surface roughness during depositional growth and sublimation of ice crystals. *Atmos. Chem. Phys.*, **18**, 13 687–13 702.

Wettlaufer, J., 2001: Dynamics of ice surfaces. *Interfacial Science*, **9**, 117–129.

Wood, S., M. Baker, and D. Calhoun, 2001: New model for the vapor growth of hexagonal ice crystals in the atmosphere. *J. Geophys. Res.*, **106**, 4845–4870.

Woods, C., M. Stoelinga, and J. Locatelli, 2007: The IMPROVE-1 storm of 1-2 February 2001. Part III: Sensitivity of a mesoscale model simulation to the respresentation of snow particle types and testing of a bulk microphysical scheme with snow habit prediction. *J. Atmos. Sci.*, **64**, 3927–3948.

Zhang, C., and J. Harrington, 2014: Including surface kinetic effects in simple models of ice vapor diffusion. *J. Atmos. Sci.*, **71**, 372–390.

LIST OF FIGURES

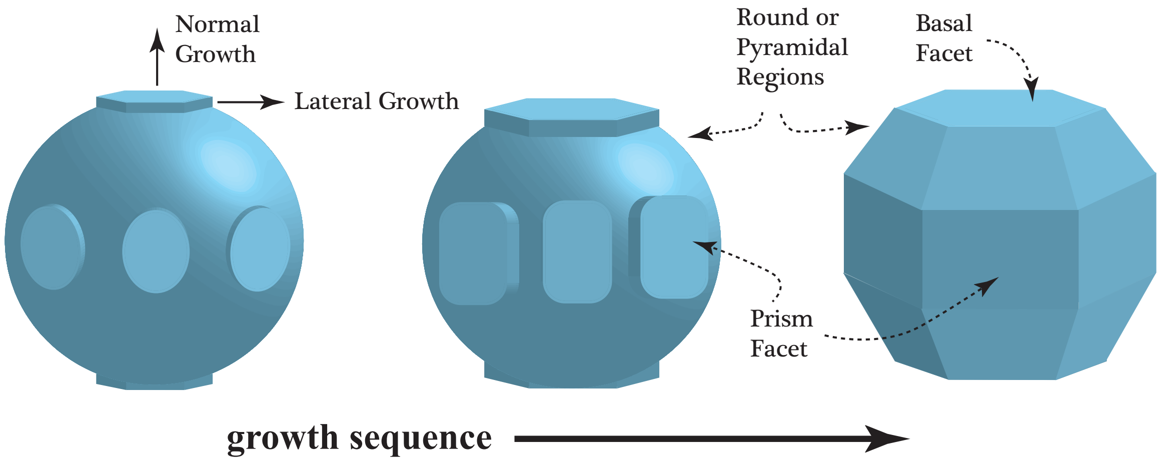

FIG. 1. Following nucleation, facets begin to develop on frozen droplets. Basal and elliptical faces appear, along with round regions or pyramidal faces. The faces grow both normally (outward) and laterally (along the surface). Over time, the elliptical regions become distinct prism, basal and pyramidal facets shown at the end. The pyramidal facets can grow themselves out of existence resulting in a hexagonal prism (not shown).

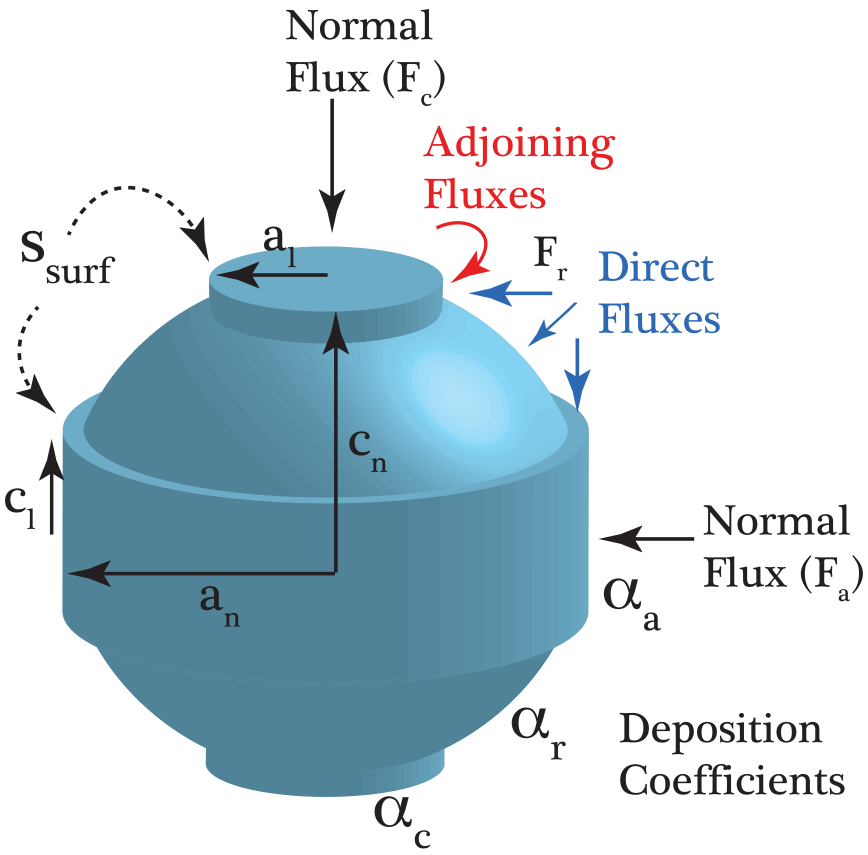

FIG. 2. Approximate model of normal and lateral growth assuming circular cylinders for the basal and prism facets. The normal fluxes (F_a and F_c) are shown along with fluxes that drive lateral growth (direct and adjoining surface, F_r), and both depend on the surface supersaturation over the facet edges, (s_{surf}). The fluxes depend on the deposition coefficients for each region, as indicated on the figure. The facets are defined in terms of their lateral dimensions, a_l for the basal facets and c_l for the prism facets. The overall crystal dimensions are given in terms of the *normal* dimensions, a_n and c_n, so named because they are perpendicular to the facet.

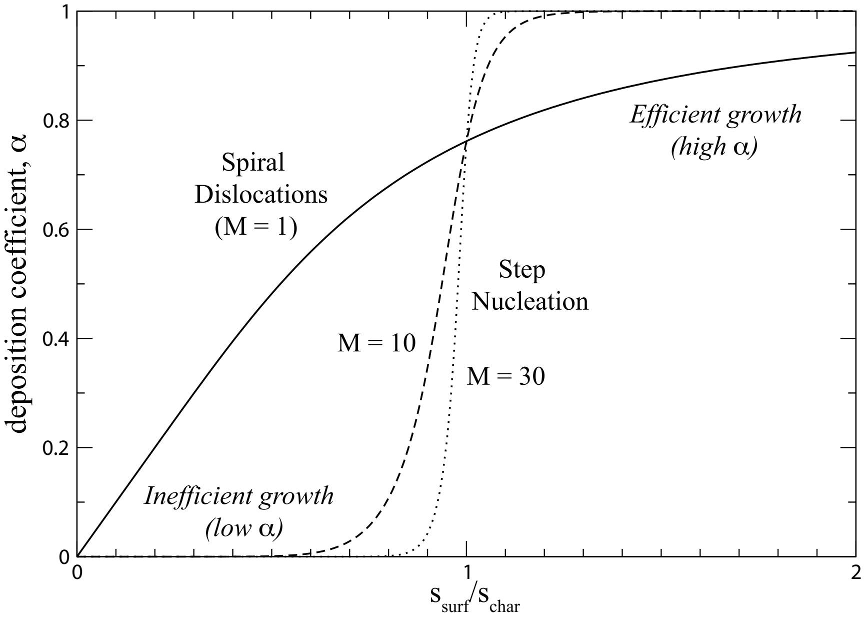

FIG. 3. Deposition coefficient as a function of the ratio of the surface to the characteristic supersaturation (s_{surf}/s_{char}) for different values of M. A value of $M = 1$ corresponds to growth by spiral dislocations whereas values of $M \geq 10$ are generally used to represent step nucleation (Nelson and Baker 1996). Spiral dislocations allow for crystal growth at low s_{surf}, unlike step nucleation which produces almost no (inefficient) growth until s_{surf} reaches s_{char} and growth rapidly becomes efficient.

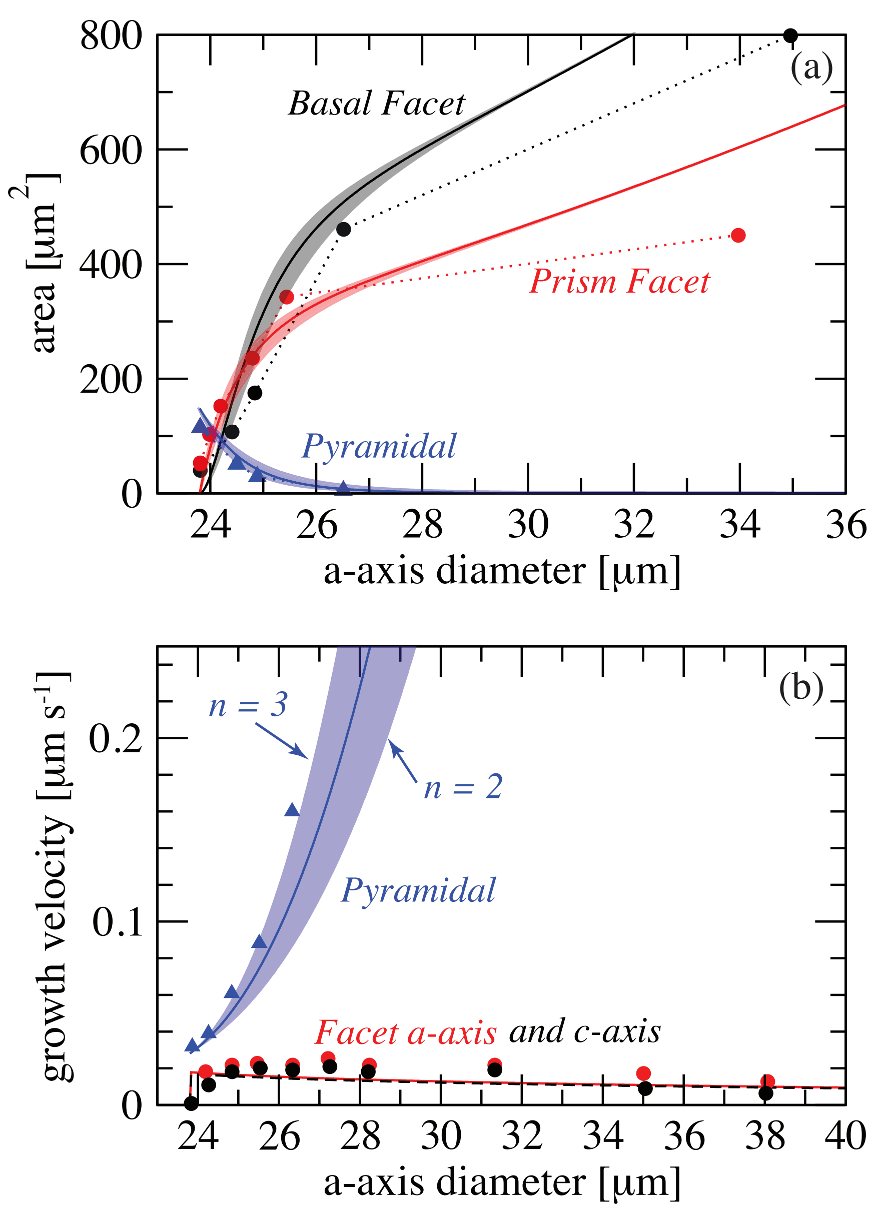

FIG. 4. (a) Area of single basal, prism, and pyramidal regions, and (b) their respective growth velocities (axis growth rates) as a function of the a-axis diameter ($2a_n$) of the crystal. The measurements of Gonda and Yamazaki (1984) are given by the symbols. The solid lines are predictions using the empirical growth model with rough area (A_r) parameterized as a ratio of the fractional volume change to the power, n with $n = 2.5$. The largest variability in the growth is due to this parameterization, with the spread indicated by the shaded regions. The upper and lower bound of each range is given by $n = 3$ and 2, respectively.

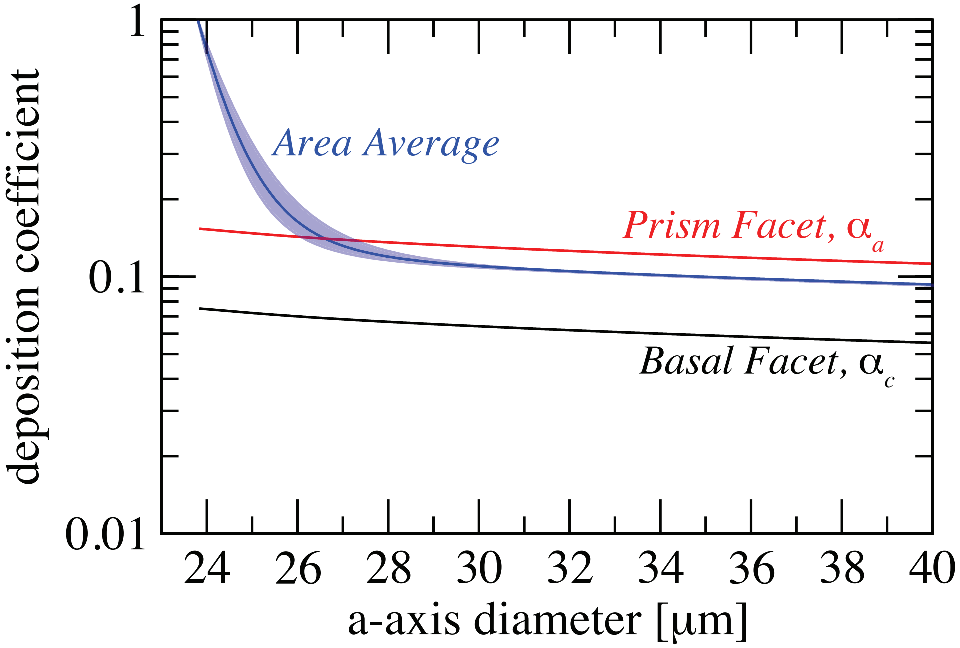

FIG. 5. Deposition coefficients as a function of the a-axis diameter ($2a_n$) for the basal facet (black), prism facet (red), and the area-weighted total (blue and blue shade). Since the total deposition coefficient is an area-weighted average, it depends on the facet and pyramidal area approximation. The blue solid line assumes $n = 2.5$ and the shaded region gives the spread in the solution for n between 2 and 3.

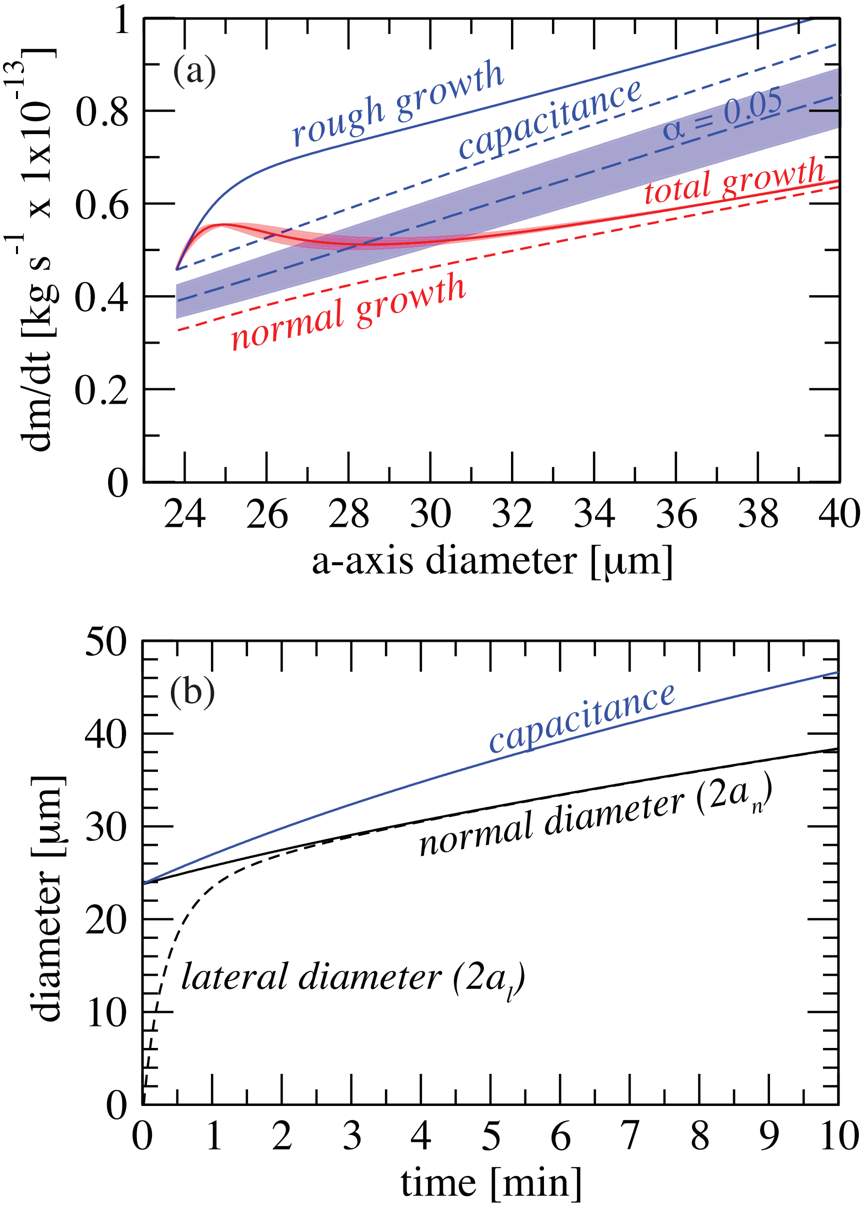

FIG. 6. (a) Mass growth rates as a function of the a-axis diameter ($2a_n$) for the total growth rate (red solid, shaded), normal growth only (red dashed), and rough growth with $\alpha = 1$ for all facets (blue solid). The solid lines use the pyramidal area (A_r) approximation with $n = 2.5$; the red shaded region shows the range of variability due to n between 2 and 3. Capacitance theory using a sphere with $\alpha = 1$ (blue short-dashed) and $\alpha = 0.05$ (blue long-dashed) is also shown, and the blue shaded region shows α ranging from 0.03 to 0.1. (b) Crystal diameters as a function of time for the lateral (black dashed) and normal (black solid) diameters along with the diameter predicted by the capacitance model ($\alpha = 1$, blue).

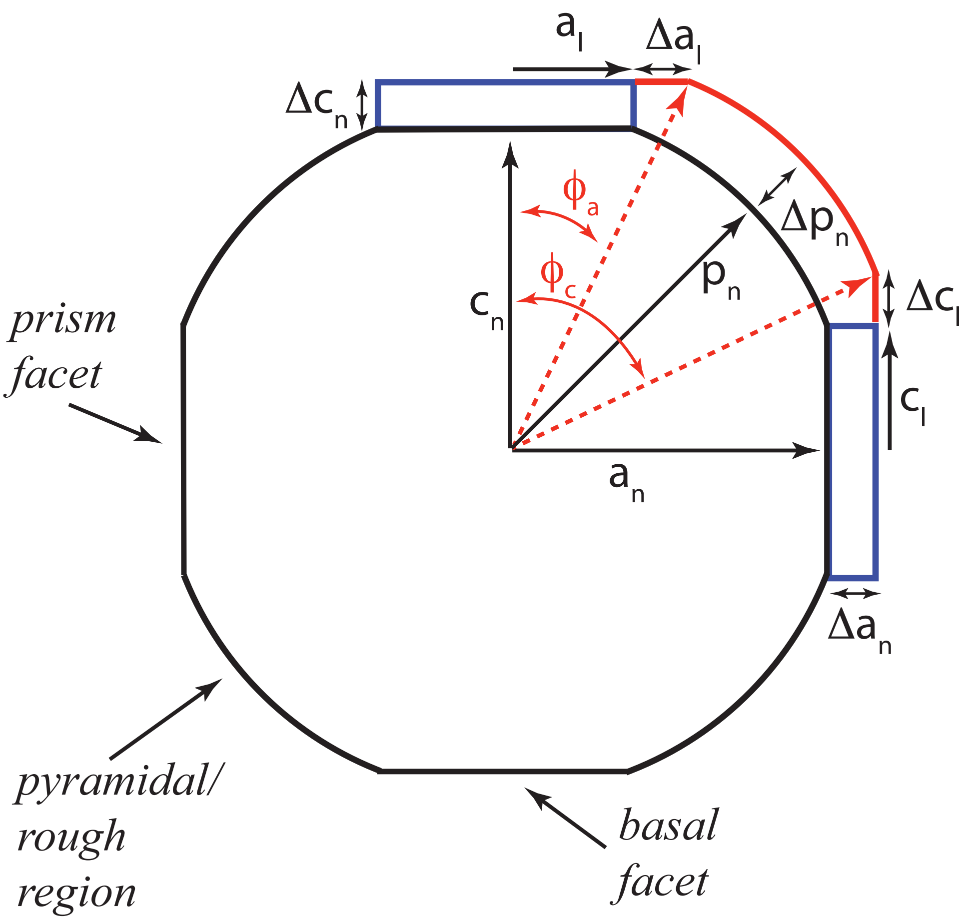

FIG. 7. Geometry for mass distribution during growth; cross-section view of Fig. 1 with the basal and prism facets flush with the round regions (no facets edges are assumed). Normal growth adds mass directly to the basal and prism facets increasing the normal lengths by Δa_n and Δc_n, indicated by the blue rectangles. Growth of the pyramidal regions (solid red outline) causes both an increase in the pyramidal length (p_n) by Δp_n, but it also causes the lateral growth of the basal and prism facets by Δa_l and Δc_l. The angles ϕ_a and ϕ_c define the location of the basal and prism intersection with the pyramidal region.

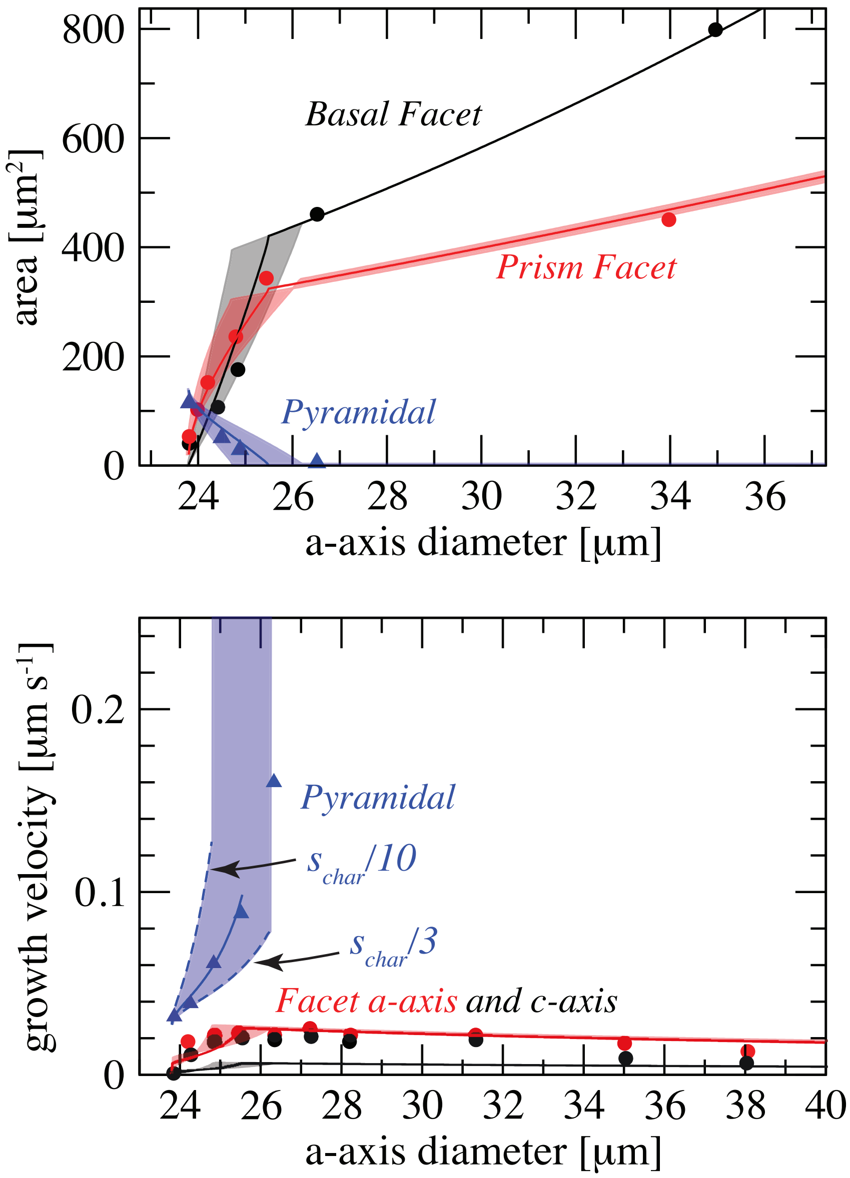

FIG. 8. (a) Area of single basal, prism, and pyramidal (rough) facets, and (b) their respective growth velocities (axis growth rates) as a function of the a-axis diameter ($2a_n$). The measurements of Gonda and Yamazaki (1984) are given by the symbols. The solid lines are predictions using the mechanistic growth theory with the pyramidal s_{char} that is a factor f_{schar} = 1/5 the value for the prism facet. The shaded ranges show the variability in the solution due to f_{schar}. The upper and lower bound of each range is given by f_{schar} = 1/10 and 1/3, respectively.

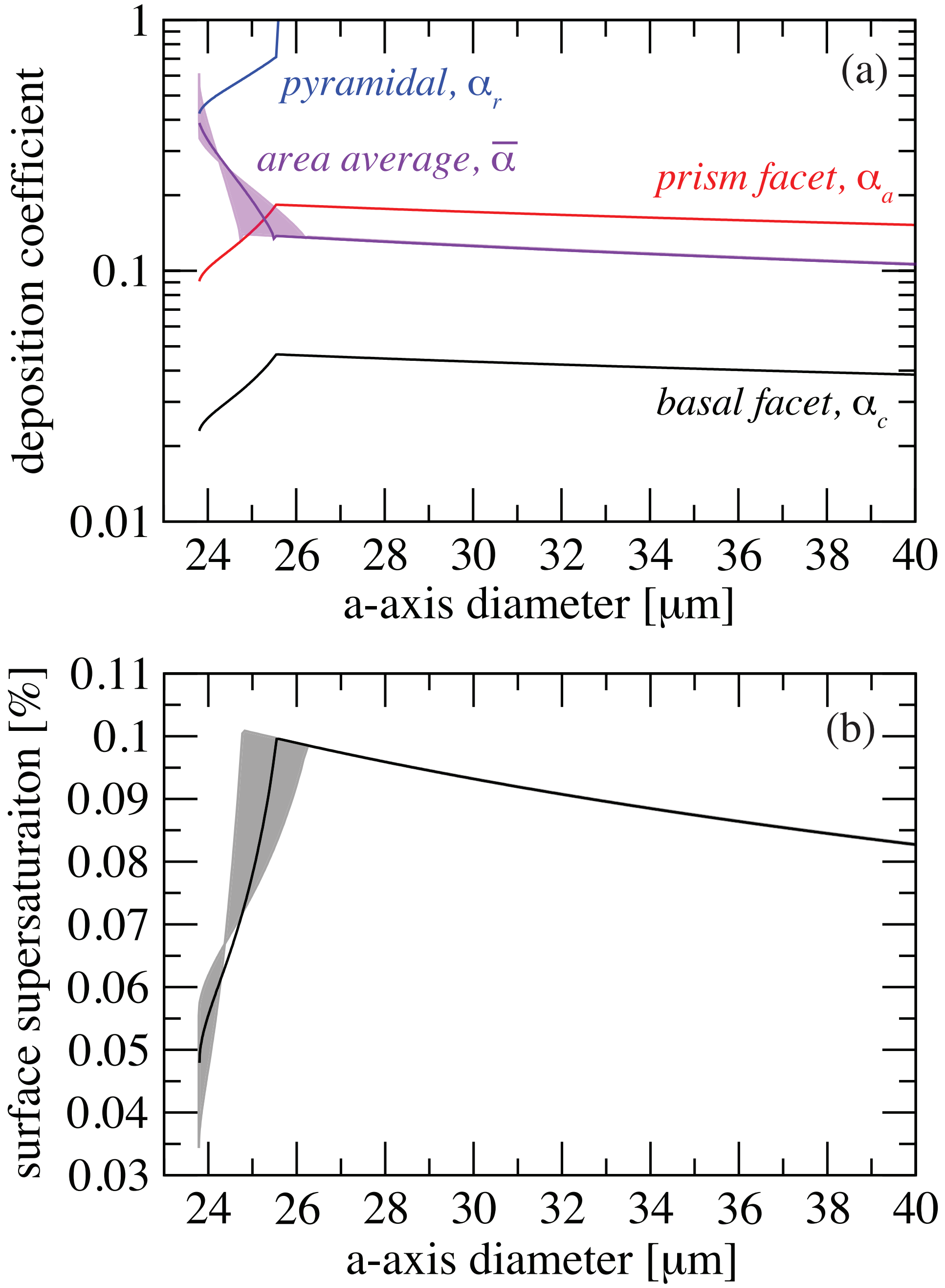

FIG. 9. (a) Deposition coefficients as a function of the a-axis diameter ($2a_n$) for the basal facet (black), prism facet (red), the pyramidal region (blue), and the area-weighted total (violet and violet shade). (b) The surface supersaturation for growth of basal, prism, and pyramidal facets (black and black shade). The solid lines assume a pyramidal s_{char} that is a factor $f_{schar} = 1/5$ the value for the prism facet, and the shaded ranges show the solution for f_{schar} ranging from 1/3 to 1/10.

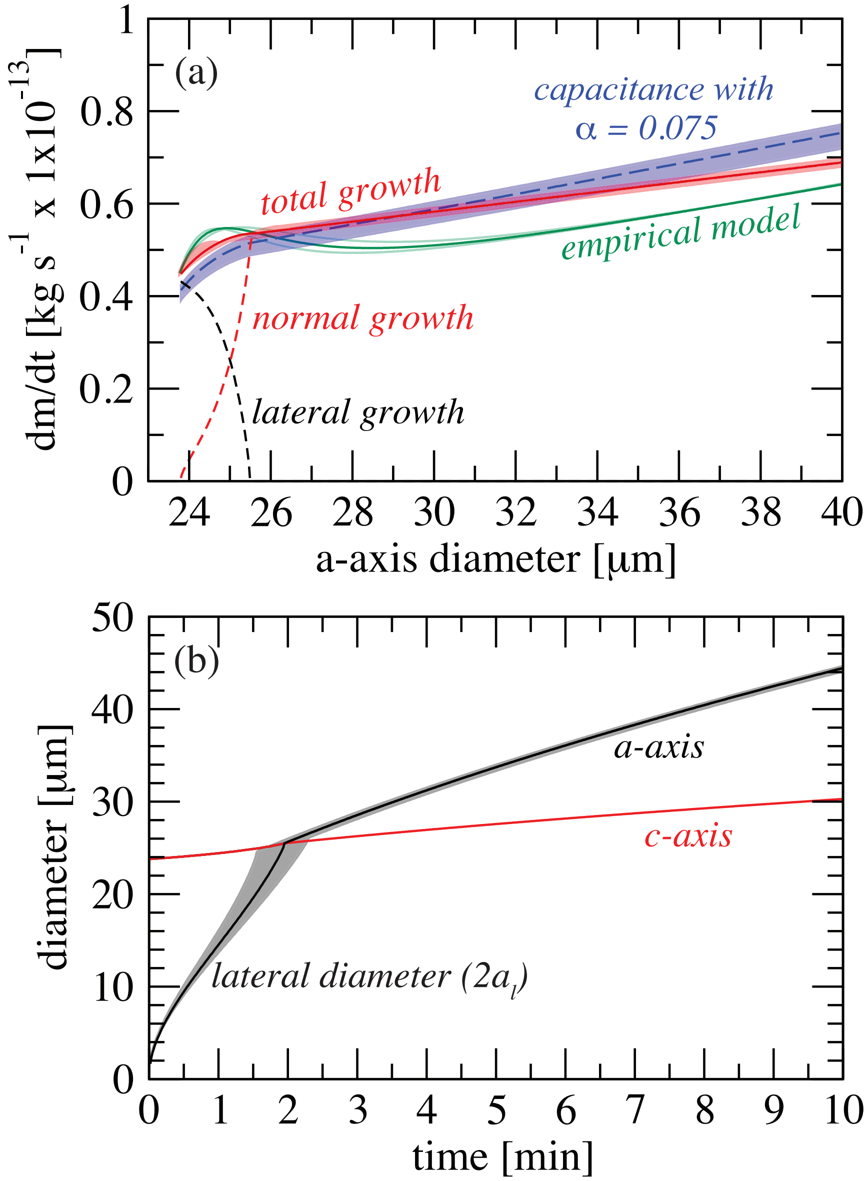

FIG. 10. (a) Mass growth rates as a function of the a-axis diameter ($2a_n$) for the total growth rate (red solid) and its components: normal growth (red dashed) and lateral growth (black dashed). The solid red line assumes a pyramidal s_{char} that is a factor f_{schar} = 1/5 the value for the prism facet, and the red shade shows the range f_{char} = 1/3 to 1/10. For comparison, the total growth rate from empirical theory (Fig. 6) is shown with the green line and shade. Capacitance theory solution using an equivalent volume sphere and a constant α of 0.075 (blue long-dashed) is also shown, and the blue shaded region shows α ranging from 0.05 to 0.1. (b) Crystal diameters as a function of time for the lateral (black) and normal a (black) and c (red) diameters. The black shade indicates the range f_{char} = 1/3 to 1/10.

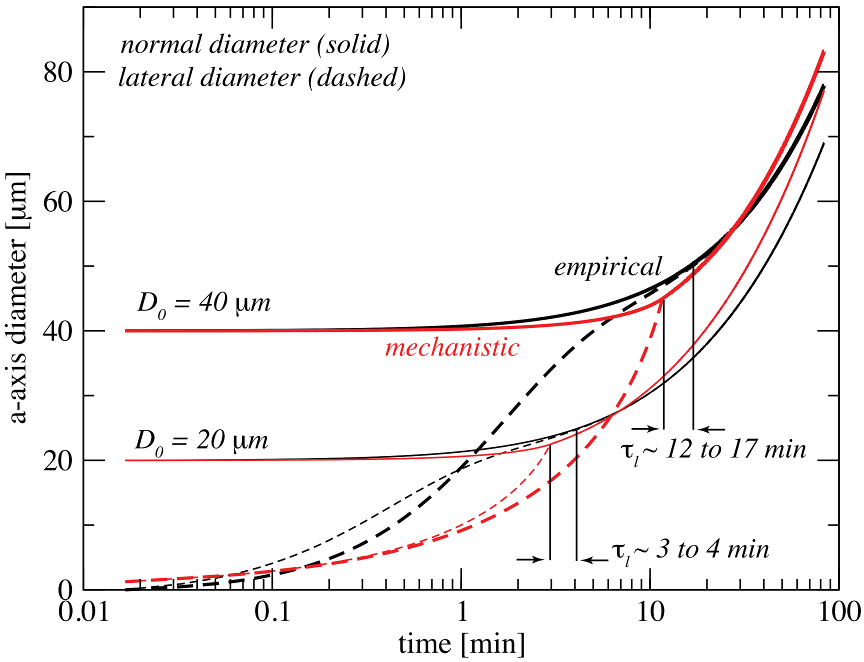

FIG. 11. Evolution of the normal (solid lines) and lateral (dashed lines) a-axis diameters in time at T = -40°C, P = 1000 hPa, and s_i = 10%. The thin and thick lines indicate an initial frozen spherical diameter of 20 and 40 μm, respectively. Solutions using the empirical model are given by the black lines whereas the mechanistic model solution is given by the red lines. The time-period for lateral growth τ_l is defined when the lateral diameter is 99% of the normal diameter, the range of τ_l given by the empirical and mechanistic models is given by the vertical solid lines. This time-scale depends strongly on the initial size.

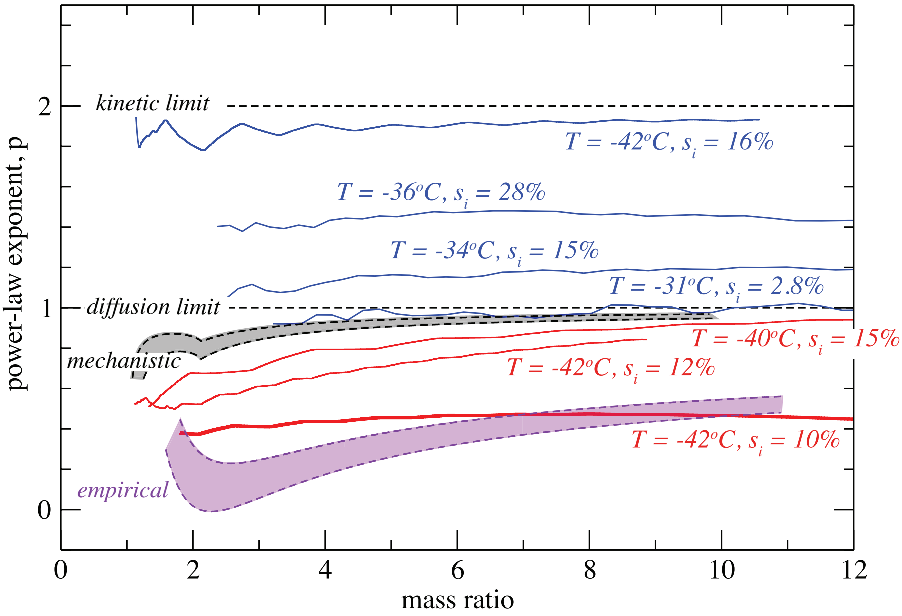

FIG. 12. Power-law exponent of the mass growth equation ($dm/dt \propto r^p$) as a function of the mass ratio (mass divided by initial mass) for vapor-grown crystals. Solid, isometric crystals undergoing normal faceted growth have values of p that range between 1 (diffusion-limited growth) and 2 (kinetics-limited growth). The solid blue (consistent with normal growth) and red (inconsistent with normal growth) curves are derived from measurements of Pokrifka et al. (2020). Solutions using the empirical and mechanistic models are indicated by the purple and black shades, respectively. The upper and lower edge of the shaded region is given by the initial particle size of $r_\circ = 10$ and 20 μm, respectively.

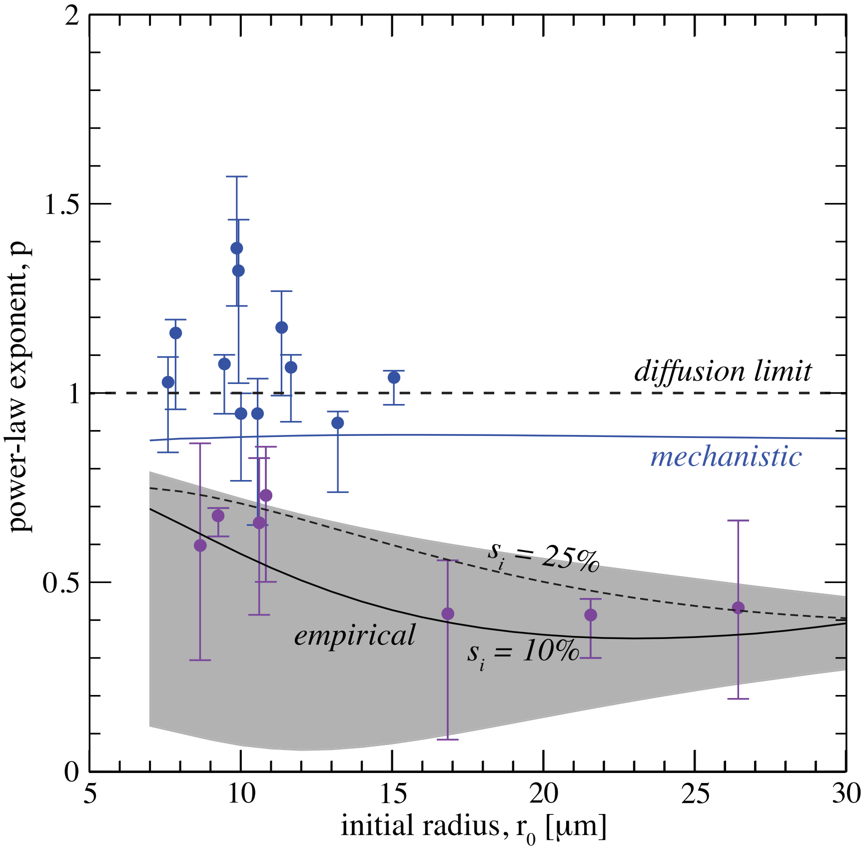

FIG. 13. Power-law exponent of the mass growth equation ($dm/dt \propto r^p$) as a function of the initial particle radius as derived from the measurements of Pokrifka et al. (2020), data points, and as calculated with the empirical (black lines) and mechanistic (blue line) models. The filled circles and lines are the average value of p, whereas the error bars and the grey shade indicate the maximum and minimum value of p attained during particle growth. The blue data points indicate growth data that could be fit with normal faceted growth, whereas purple points required a model of faceting transitions. The black solid and dashed curves indicate the model solution supersaturation dependence (10 and 25%, respectively), and this range was chosen based on the measurement range.

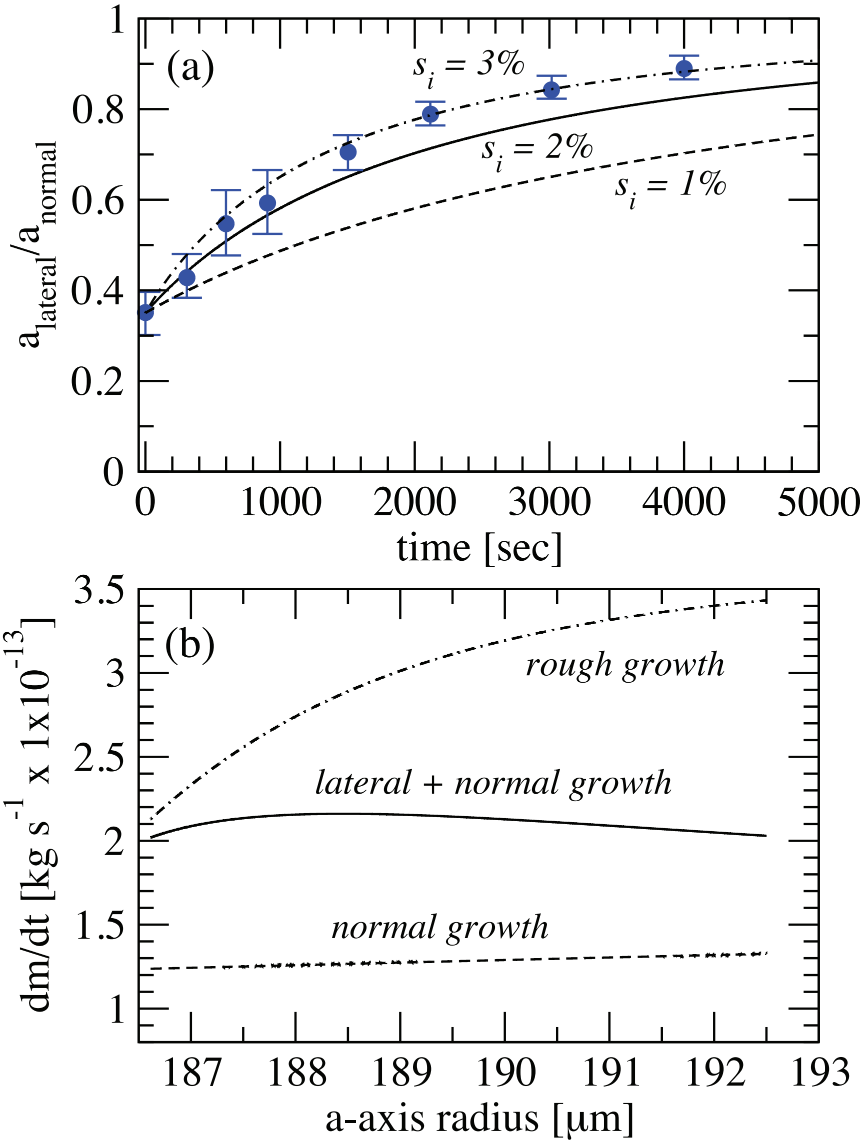

FIG. 14. (a) Ratio of the lateral and normal a-axis lengths as a function of time. The blue data points are from Fig. 6 of Nelson and Swanson (2019) who measured the lateral basal facet spreading of a planar crystal with an a-axis radius of about 165 μm at T = -30°C and at a supersaturation of 1%. Empirical model solutions for an initially spheroidal crystal with no facets, a thickness of 60 μm, and supersaturations of 1, 2 and 3% are shown by the solid lines. (b) The total mass growth rate (normal and lateral, solid line) as a function of the normal a-axis radius. The growth rate computed as if the particle were rough ($\alpha = 1$, dot-dashed line) or undergoing only normal faceted growth (dashed line) are also shown.